The Infall Motion in the Low-mass Protostellar Binary NGC 1333 IRAS 4A1/4A2

Yu-Nung Su¹, Sheng-Yuan Liu¹, Zhi-Yun Li², Chin-Fei Lee¹, Naomi Hirano¹, Shigehisa Takakuwa^{1,3}, and I-Ta Hsieh¹ Institute of Astronomy and Astrophysics, Academia Sinica, 11F of ASMAB, AS/NTU No.1, Sec. 4, Roosevelt Road, Taipei 10617, Taiwan ² Department of Astronomy, University of Virginia, Charlottesville, VA 22904, USA

³ Department of Physics and Astronomy, Graduate School of Science and Engineering, Kagoshima University, 1-21-35 Korimoto, Kagoshima 890-0065, Japan Received 2019 July 7; revised 2019 September 24; accepted 2019 September 24; published 2019 November 5

Abstract

We report ALMA observations of NGC 1333 IRAS 4A, a young low-mass protostellar binary, whose components are referred to as 4A1 and 4A2. With multiple H_2CO transitions and HNC (4-3) observed at a resolution of 0."25 (~70 au), we investigate the gas kinematics of 4A1 and 4A2. Our results show that on the large angular scale (~10"), 4A1 and 4A2 each display a well-collimated outflow along the N-S direction, and an S-shaped morphology is discerned in the outflow powered by 4A2. On the small scale (~0."3), 4A1 and 4A2 exhibit distinct spectral features toward the continuum centroid, with 4A1 showing simple symmetric profiles predominantly in absorption and 4A2 demonstrating rather complicated profiles in emission as well as in absorption. Based on radiative transfer modeling exercises, we find that the physical parameters inferred from earlier low-resolution observations cannot be directly extrapolated down to the inner region of 4A1. Possible reasons for the discrepancies between the observed and modeled profiles are discussed. We constrain the mass infall rate in 4A1 to be at most around 3 × 10⁻⁵ M_{\odot} yr⁻¹ at the layer of 75 au. For the kinematics of the inner envelope of 4A2, the absorbing dips in the H_2CO spectra are skewed toward the redshifted side and likely signatures of inward motion. These absorbing dips are relatively narrow. This is, like the case for 4A1, significantly slower than the anticipated inflow speed. We estimate a mass infall rate of $(3.1-6.2) \times 10^{-5} M_{\odot}$ yr⁻¹ at the layer of 100 au in 4A2.

Unified Astronomy Thesaurus concepts: Star formation (1569)

1. Introduction

Although gravitational collapse of molecular gas has been widely accepted from the theoretical viewpoints of star formation, acquiring direct observational evidence of gas infall motions poses a challenge (Myers et al. 2000; Evans et al. 2015). Based on single-dish observations, infall motions are generally inferred from asymmetric blue profiles of optically thick lines (e.g., Mardones et al. 1997). Such kinematic features at relatively low velocity, however, are easily contaminated by other star formation activities such as outflows, rotation, and turbulence. Another diagnostic of infall motion is the triangular-like position-velocity structure in both blue- and redshifted sides (Ohashi et al. 1997). These types of positionvelocity structure have been reported in several low-mass starforming regions (e.g., HH 211, HH 212, and L1527), and this structure is interpreted as the result of an infalling-rotating envelope (Sakai et al. 2014; Lee et al. 2017, 2019).

The "inverse P-Cygni" line profile, i.e., the redshifted selfabsorption of spectral lines, is considered as a more robust probe of infall motions. Envelope material in front that moves inward toward the central (continuum) source causes the redshifted absorption. The absorption signature is easier to discern with observations at higher frequencies because the intensity of the dust continuum increases rapidly with frequency. Indeed, high-frequency (~1 THz) observations with SOFIA and Herschel have identified redshifted absorption features toward several star formation regions (Wyrowski et al. 2012; Mottram et al. 2013). With angular resolutions of 15"-30", however, these studies cannot resolve the kinematics in the inner infalling envelope. For freefall inward motion (i.e., $v_{\rm infall} \propto r^{-1/2}$), one would expect a higher infalling velocity closer to the central object. Such high-velocity infalling gas cannot be readily discerned with single-dish observations due to its relatively small filling factor. The fact that the dust

continuum could become optically thick at high-frequency regimes, in particular in the inner region, will further complicate the detection of high-velocity infalling gas. Interferometric observations at millimeter and submillimeter wavelengths serve as another channel to probe infalling gas (e.g., Di Francesco et al. 2001). With high sensitivity and angular resolution, ALMA provides an invaluable opportunity for studying inward motion in molecular lines with their absorption signature against the continuum. For example, recent ALMA 690 GHz observations of IRAS 16293-2422B at 0"2 resolution revealed pronounced inverse P-Cygni profiles, with faster infalling gas located closer to the central object (Zapata et al. 2013). Observations of the low-mass protostar B335 with ALMA at 0."5 resolution also identified redshifted absorption features against the continuum in HCN and HCO⁺ lines (Evans et al. 2015).

Located at a distance of 293 pc in the Perseus star formation complex (Ortiz-León et al. 2018; Zucker et al. 2018), NGC 1333 IRAS 4A (hereafter IRAS 4A) is one of the brightest dust continuum sources among low-mass protostars (Looney et al. 2000). Single-dish observations of IRAS 4A with millimeter and submillimeter transitions revealed asymmetric blue profiles of optically thick lines relative to symmetric optically thin transitions, suggestive of infall motions in this region (e.g., Blake et al. 1995; Belloche et al. 2006). The inverse P-Cygni profiles toward IRAS 4A were obtained in $H_2CO(3_{12}-2_{11})$ as well as CS (3-2) and N_2H^+ (1-0) at $\sim 2''$ resolution with the Plateau de Bure Interferometer (PdBI; Di Francesco et al. 2001). This detection provided the least ambiguous evidence of infall motions in this region to date, although the possibility of the absorption features being caused by an unrelated foreground absorption layer cannot be completely ruled out (for a comprehensive discussion, see Choi et al. 2004). Observations of polarized dust emission with the SMA have revealed a clear

Table 1
Expected Transitions

Lines in LSB			Lines in USB			
Transition	Frequency (GHz)	Energy Level (K)	Transition	Frequency (GHz)	Energy level (K)	
H ₂ CO (5 ₁₅ -4 ₁₄)	351.76864	$E_u = 62.5 \text{ K}$	H ₂ CO (5 ₀₅ -4 ₀₄)	362.73605	$E_u = 52.3 \text{ K}$	
			$H_2CO (5_{24}-4_{23})$	363.94589	$E_u = 99.5 \text{ K}$	
			$H_2CO (5_{41}-4_{40})$	364.10325	$E_u = 240.7 \text{ K}$	
			$H_2CO(5_{33}-4_{32})$	364.27514	$E_u = 158.4 \text{ K}$	
			$H_2CO(5_{32}-4_{31})$	364.28888	$E_u = 158.4 \text{ K}$	
			HNC (4-3)	362.63030	$E_u = 43.5 \text{ K}$	

hourglass-shaped B-field toward IRAS 4A (Girart et al. 2006). The estimated mass-to-magnetic flux ratio implies that the region traced by the SMA is slightly supercritical. Gonçalves et al. (2008) modeled the observed magnetic field in this region and concluded that the magnetic field morphology in IRAS 4A is consistent with the standard theoretical scenario for the formation of low-mass stars from cores threaded by ordered rather than turbulent magnetic fields.

IRAS 4A has been resolved into two separated sources (whose components are referred to as 4A1 and 4A2, with an angular separation of 1"8) at high-resolution millimeter and submillimeter maps (e.g., Looney et al. 2000; Jørgensen et al. 2007; Chen et al. 2013). The two cores, 4A1 and 4A2, each drive a well-collimated outflow/jet along the N-S direction (Choi 2005; Santangelo et al. 2015). Very Large Array (VLA) observations of the NH₃ (2,2) and (3,3) lines revealed a rotating disk toward 4A2 only (Choi et al. 2010). In contrast, the nature of the NH₃ lines toward 4A1 is less clear. It could be a mixture of a circumstellar disk and a molecular outflow (Choi et al. 2011). With high-resolution 8 mm VLA dust continuum observations, the recent VANDAM survey produced disk-fit results of 4A1 in the visibility domain (Segura-Cox et al. 2018). As signposts of hot corinos, complex molecules (e.g., HCOOCH₃, HCOOH, and CH₃CN) have been detected toward IRAS 4A by the IRAM 30 m Telescope (Bottinelli et al. 2004). Recent interferometric observations with ALMA and the PdBI further resolved the distributions of these complex species, with 4A2 demonstrating a chemically rich spectrum and 4A1 lacking detections of most complex organic molecules (COMs; Santangelo et al. 2015; Taquet et al. 2015; López-Sepulcre et al. 2017). Based on the different properties of the molecular outflows and the central driving sources, Santangelo et al. (2015) argued different evolutionary stages for 4A1 and 4A2, with 4A1 being younger than 4A2. A similar conclusion was also reached by Choi et al. (2010) with the VLA observations in NH₃ and SiO.

Here we present newly obtained ALMA observations in multiple $\rm H_2CO$ transitions and of HNC (4–3) at a resolution of 0."25 (corresponding to a linear scale of ~70 au at a distance of 293 pc) to illustrate the gas kinematics around the two dense cores 4A1 and 4A2 on scales of 70–350 au. The obtained ALMA data sets also contain rich information in chemistry, and the chemical behaviors of 4A1 and 4A2 have been discussed in Sahu et al. (2019), with their main finding in the firm identification, for the first time, of COMs, including CH₃OH, 13 CH₃OH, CH₂DOH, and CH₃CHO, associated with the 4A1 core in absorption. Our ALMA observations to date provide the data with the best spatial resolution to discriminate the gas kinematics between 4A1 and 4A2. We note that the $\rm H_2CO$ and HNC data presented here have a velocity resolution

of $\sim 0.12 \,\mathrm{km \, s^{-1}}$, which is about a factor of 8 better than the data presented by Sahu et al. (2019).

2. Observations and Data Reduction

Observations of NGC 1333 IRAS 4A with ALMA in band 7 (i.e., the 350 GHz band) were carried out using its 12 m array in its C40-3 and C40-5 configurations under the project code 2015.1.00147.S. For the observations in the C40-5 configuration, two executions were carried out on 2016 July 23 and 24, with 39 and 42 antennas in the array, respectively. Each execution has an on-source time of about 28 minutes, and the projected baseline lengths range from 15.4 to 1100 m. For the observations in the C40-3 configuration, a single execution was obtained on 2016 December 14, with 43 antennas in the array. The on-source integration time of the C40-3 execution is also about 28 minutes, and the projected baseline lengths range from 12.3 to 382 m. The phase center in the ICRS reference frame was R.A. = $03^{\text{h}}29^{\hat{\text{m}}}10^{\hat{\text{s}}}50$ and decl. = $+31^{\circ}13'31''50$ (J2000). The half-power width of the ALMA 12m antenna primary beam was ~ 16.55 at 351.7 GHz, which is more than sufficient to cover the entire extents of the 4A1 and 4A2 cores.

The ALMA band 7 receivers were used to simultaneously capture six H₂CO transitions whose upper energy levels range from approximately 50 to 240 K and HNC (4-3), as summarized in Table 1. For each transition, the ALMA correlator was configured to provide a velocity resolution of about 0.12 km s⁻¹ and a total bandwidth of either 58.6 MHz $(\sim 50 \text{ km s}^{-1})$ or 117.2 MHz $(\sim 100 \text{ km s}^{-1})$. A broadband spectral window of 1.875 GHz centered at 350.7 GHz with a resolution of 1.13 MHz (0.965 km s⁻¹) was also included, and the results of the broadband window data have been presented in Sahu et al. (2019). Quasars J0238+1636 and J0510+1800 were observed to calibrate the passband, and Ceres and quasars J0006-0623 and J0510+1800 were observed to calibrate the absolute flux scale. The quasar J0336+3218 was observed as the gain calibrator. The acquired visibility data were reduced using the observatory pipeline in CASA (Common Astronomy Software Application; McMullin et al. 2007) version 4.7.0. We then generated both the 0.84 mm continuum and spectral visibilities by fitting and subtracting continuum emission in the visibility domain. The calibrated visibility data were Fouriertransformed and CLEANed with CASA 4.7.0 also. By using Briggs weighting with a robust parameter of 0.5, we obtained a synthesized beam size of about 0.31×0.20 at P.A. of -6° 0. We smoothed our data to a resolution of 0.15 km s⁻¹ for the analysis presented below. The typical rms noise level in the maps is about 6-8 mJy beam⁻¹ ($\sim 0.95-1.20 \,\mathrm{K}$) in a $0.15 \, \mathrm{km \, s^{-1}}$ bin. We note that given the existence of the absorption features (see Section 4.2), a preferred approach of a

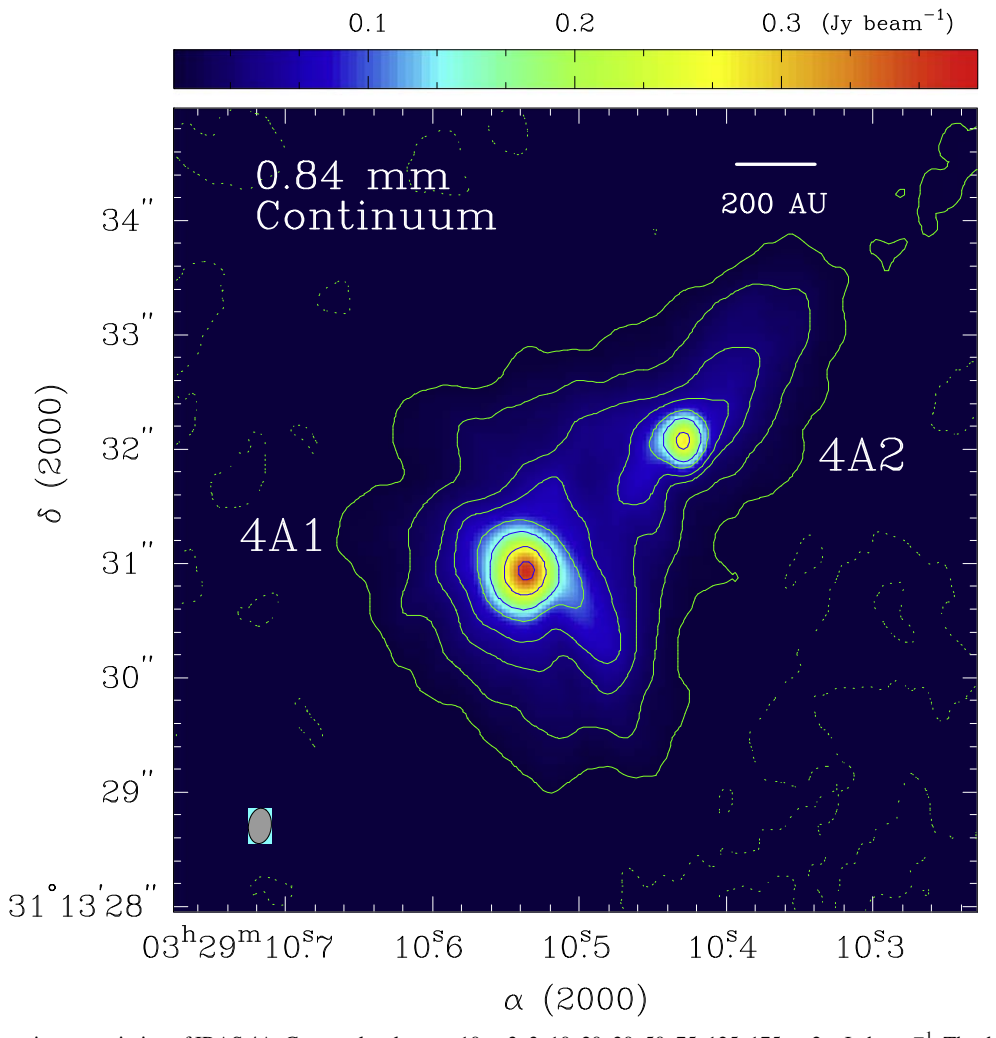


Figure 1. The 0.84 mm continuum emission of IRAS 4A. Contour levels are -10, -3, 3, 10, 20, 30, 50, 75, 125, 175×2 mJy beam $^{-1}$. The dark ellipse in the bottom left corner denotes the synthesized beam of $0\rlap.''31 \times 0\rlap.''20$ at P.A. $-6\rlap.^\circ45$. Note that due to the existence of bright sources, the continuum map is limited by dynamic range rather than sensitivity.

CLEAN algorithm is to perform continuum subtraction after CLEANing in order to avoid using CLEAN on a cube, where both emission and absorption are present. The images made with these two approaches, however, do not exhibit a notable difference in line features. In particular, the shapes of the spectral profiles toward 4A1 and 4A2 made with these two CLEAN approaches are almost identical.

3. The 0.84 mm Continuum Emission

Figure 1 shows the 0.84 mm (357 GHz) continuum image toward IRAS 4A. At an angular resolution of $0.''31 \times 0.''20$, IRAS 4A is clearly resolved into two components, with 4A1 located in the SE and 4A2 in the NW. The brightness temperatures inferred from the observed peak continuum are 57 K and 42 K toward 4A1 and 4A2, respectively. Note that these brightness temperatures are the beam-averaged values, and the actual peak brightness temperatures at smaller scales could be higher. 4A1 and 4A2 each appear to consist of a compact core and an extended outer envelope. The results of the 2D Gaussian fits as well as the estimated mass of each component can be found in Table 1 of Sahu et al. (2019). With the optically thin assumption, the authors estimated the dust and gas mass to be 0.15 M_{\odot} , 0.49 M_{\odot} , 0.07 M_{\odot} , and 0.50 M_{\odot} for the 4A1

compact component, 4A1 extended component, 4A2 compact component, and 4A2 extended component, respectively. As concluded by Sahu et al. (2019), the 0.84 mm dust emission from the 4A1 core is optically thick and 4A2 is predominantly optically thin. With multifrequency polarization observations, Ko et al. (2019) also conclude that the dust continuum at the innermost area of 4A1 is optically thick at wavelengths shorter than $\sim\!1.5$ mm. As a consequence, the estimated mass for the 4A1 compact component could be significantly underestimated. Sahu et al. (2019) also derived the molecular hydrogen column density toward the 4A1 centroid to be at least $1.3\times10^{26}\,\mathrm{cm}^{-2}$. We note that in addition to the above-mentioned compact and extended components, several spur-like structures can be discerned in the 0.84 mm continuum emission. The most evident spur is that located to the southwest of 4A1.

4. H₂CO and HNC (4-3) Features

The spectral data cubes of the H_2CO and HNC (4–3) lines exhibit both compact features associated with 4A1 and 4A2 and extended structures in the vicinity of IRAS 4A. Determining the systemic velocities of both 4A1 and 4A2 is an essential step for a proper understanding of the observed kinematic features. Di Francesco et al. (2001) estimated a systemic velocity of

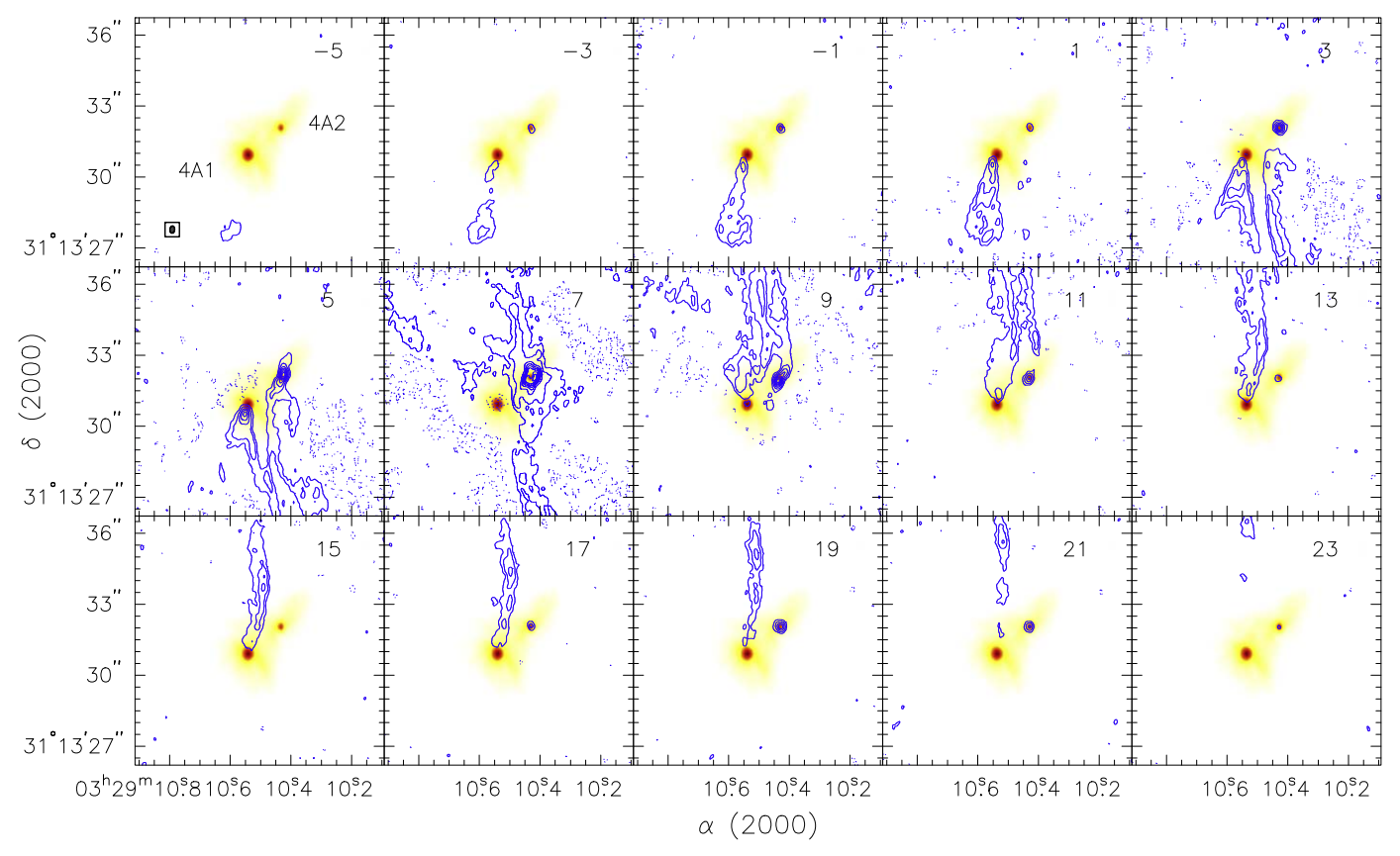


Figure 2. Channel maps of IRAS 4A in H_2CO 5_{05} – 4_{04} . The local standard of rest (LSR) velocity of each channel is indicated in the upper right corner of each panel. The LSR velocity of the system is 6.95 km s⁻¹. Solid contours are at 4, 10, 20, 30, 40, 50, 60 and 70×3 mJy beam⁻¹, and dotted contours indicate -4, -10, -20, and -30×3 mJy beam⁻¹. For each panel, the overlaid color scales are the 0.84 mm continuum emission shown in Figure 1. The dark ellipse in the bottom left corner of the first panel denotes the synthesized beam. The compact component located at the 4A2 continuum peak detected from 17 to 23 km s⁻¹ is likely not related to the H_2CO 5_{05} – 4_{00} outflowing gas but comes from contamination of other molecular species because 4A2 is a known hot-corino object.

 Table 2

 Molecular Transitions Detected toward IRAS 4A1 and 4A2

Transition	E_u (K)	Peak Intensity (Jy beam ⁻¹)	$V_{\rm LSR}$ (km s ⁻¹)	$\frac{\Delta V}{(\text{km s}^{-1})}$	Peak Intensity (Jy beam ⁻¹)	$V_{\rm LSR}$ (km s ⁻¹)	$\frac{\Delta V}{(\text{km s}^{-1})}$	
		Transit	tions toward IRAS 4	A1	Transitions toward IRAS 4A2			
HNC (4-3)	43.5	-0.417 (0.009)	7.25 (0.01)	1.16 (0.03)	0.214 (0.009)	6.99 (0.06)	4.26 (0.19)	
$H_2CO (5_{05}-4_{04})$	52.3	-0.205 (0.016)	6.96 (0.03)	0.81 (0.07)	0.309 (0.008)	7.05 (0.03)	4.08 (0.10)	
$H_2CO (5_{15}-4_{14})$	62.5	-0.273 (0.014)	6.98 (0.02)	0.99 (0.06)	0.290 (0.007)	6.96 (0.04)	4.20 (0.10)	
$H_2CO (5_{24} - 4_{23})$	99.5	-0.091 (0.017)	6.88 (0.07)	0.80 (0.17)	0.318 (0.007)	7.01 (0.03)	3.87 (0.07)	
H ₂ CO (5 ₃₃ -4 ₃₂)	158.4	-0.079(0.015)	6.78 (0.09)	0.98 (0.22)	0.312 (0.010)	7.02 (0.05)	4.29 (0.12)	
$H_2CO (5_{32}-4_{31})$	158.4	-0.071 (0.016)	6.81 (0.10)	0.90 (0.23)	0.307 (0.008)	6.96 (0.04)	4.17 (0.11)	
$H_2CO (5_{41} - 4_{40})$	240.7	$-0.053 \; (0.015)$	6.76 (0.14)	0.99 (0.32)	0.278 (0.010)	6.98 (0.04)	3.68 (0.11)	

 $6.95~\rm km~s^{-1}$ for the IRAS 4A system as a whole. 4A1 and 4A2, however, may have (slightly) different systemic velocities. Using the average fitted peak velocity of the six observed H₂CO transitions (see Table 2 as well as Sections 4.2.1 and 4.2.2), we adopt systemic velocities of $6.86~\rm km~s^{-1}$ and $7.00~\rm km~s^{-1}$ for 4A1 and 4A2, respectively. Note that the blue- and redshifted motions mentioned in the following sections are relative to the abovementioned systemic velocities. We present below the results of the spectral line features from the large to the small angular scale.

4.1. Molecular Outflows

The most noticeable extended structures are the two collimated molecular outflows, which can be discerned in all the observed H_2CO transitions as well as in HNC (4–3), powered by 4A1 and 4A2. Figure 2 shows the channel maps of the H_2CO 5_{05} – 4_{04} line toward IRAS 4A. For display purposes, we have smoothed the channel maps to a velocity resolution of 2 km s^{-1} . Figure 3 displays the integrated blue- and redshifted emission of H_2CO 5_{05} – 4_{04} , 5_{24} – 4_{23} , and 5_{15} – 4_{14} . For both figures, two well-collimated outflows along the N–S direction at \sim 8" scale are visible. The 4A1 outflow seen in H_2CO 5_{05} – 4_{04} is detected to relative velocities of about 12 km s^{-1} and 16 km s^{-1} in its blue- and redshifted components, respectively. In contrast, the H_2CO 5_{05} – 4_{04} outflowing gas powered by 4A2 is only detected up to \sim 5 km s⁻¹ in relative velocity. Note that the lack of emission features toward the centroid of 4A1 in

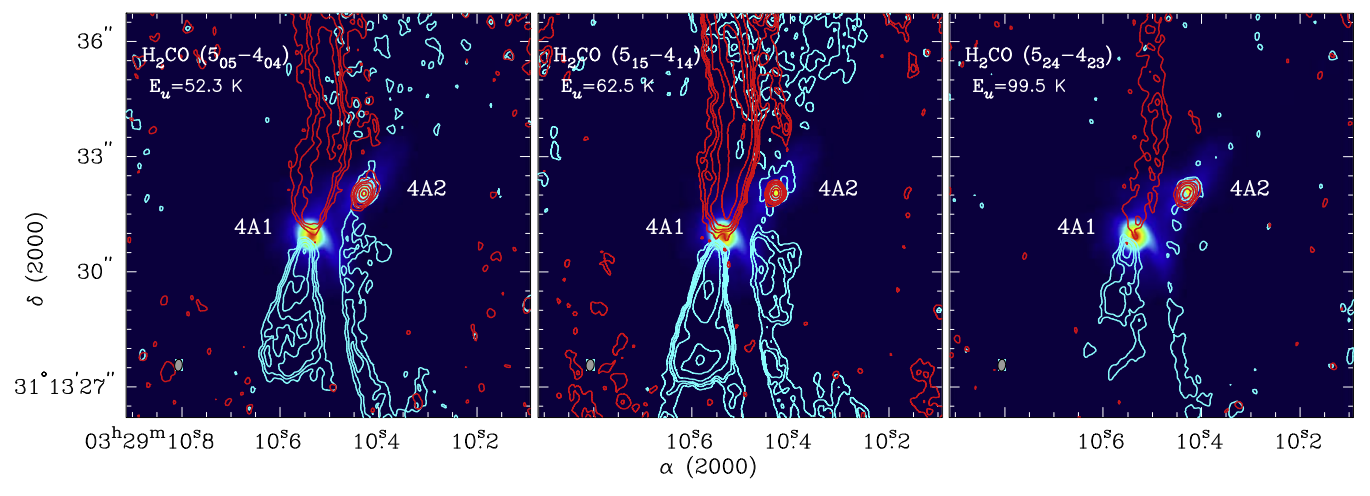


Figure 3. Bipolar molecular outflows of H_2CO 5_{05} – 4_{04} (left), 5_{15} – 4_{14} (middle) and 5_{24} – 4_{23} (right) toward IRAS 4A. In each panel, the color scales present the 0.84 mm continuum shown in Figure 1 and the dark ellipse in the bottom left corner denotes the synthesized beam.

Figures 2 and 3 also implies that its 0.84 mm continuum is optically thick.

The low-velocity blueshifted H₂CO component associated with 4A1 exhibits a conical shell-like structure opening to the south-southeast. In contrast, the high-velocity blueshifted component shows a jet-like structure. Such distinct morphologies in low- and high-velocity components have been detected in several low-mass outflows such as those from HH211 and IRAS 04166+2706 (Gueth & Guilloteau 1999; Santiago-García et al. 2009). Regarding the redshifted component of the 4A1 outflow, no clear conical structure can be discerned, perhaps due to contamination or overlap with the 4A2 outflow. Our observations also detect in the $H_2CO\ 5_{15}-4_{14}$ and $5_{33}-4_{32}$ emission the two extremely high-velocity (EHV) redshifted knots 2''-4'' from the core, with velocities (V_{LSR}) in the range of 35–55 km s⁻¹ that are associated with 4A1, as previously reported by Santangelo et al. (2015). For the other observed H_2CO transitions as well as HNC (4-3), the spectral windows were not wide enough to capture the redshifted EHV components.

For the 4A2 H_2CO outflow, bending (or S-shaped) morphologies can be discerned in both the blue- and redshifted components. The bending structure has previously been identified in CO (2–1) and SiO (5–4) with the PdBI observations (Santangelo et al. 2015). Within \sim 8" in radius of 4A2, Santangelo et al. (2015) reported a collimated outflow along the N–S direction. A sharp bend can be found at a distance of about 4" away from the driving source, with the outflow direction changing to NW–SE. The authors interpreted this sharp bend as resulting from outflow precession, and estimated jet precession on very short timescales of \sim 200–600 yr. Instead of a well-collimated morphology, our H_2CO maps further reveal a gradual change of the outflow direction in the close vicinity of 4A2.

4.2. Dense Gas Associated with a Disk and Envelope

Figure 4 shows the observed spectra of the six H₂CO lines as well as HNC (4-3) at the pixel where the 0.84 mm continuum peaks at 4A1 (left) and 4A2 (right). Although toward both sources all targeted H₂CO and HNC transitions are clearly detected, 4A1 and 4A2 exhibit distinct spectral features, with 4A1 showing simple symmetric profiles predominantly in

absorption and 4A2 demonstrating relatively complicated profiles in emission as well as in absorption.

4.2.1. The Line Feature toward 4A1

The absorption profiles of the $\rm H_2CO$ and HNC transitions detected toward the 4A1 centroid appear to be Gaussian-like. We performed Gaussian profile fitting to extract the line parameters. The fitting profiles are overlaid in the left panel of Figure 4, and the fitting results are summarized in Table 2. The 4A1 systemic velocity of $6.86\,\rm km\,s^{-1}$ estimated from the average fitted peak velocity of the six observed $\rm H_2CO$ transitions is also labeled in Figure 4. The line widths of the $\rm H_2CO$ transitions range from 0.80 to 0.99 km s⁻¹, and their central line velocities ($V_{\rm LSR}$) are consistent with each other, i.e., in the range of 6.76– $6.98\,\rm km\,s^{-1}$.

With a broader line width of 1.16 km s⁻¹ and a redshifted central line velocity of 7.25 km s⁻¹, the absorption feature of HNC (4-3) is different from the above-mentioned H₂CO transitions. Unlike the compact (<1") H₂CO absorption features detected toward 4A1 (see below), the absorption seen in HNC (4-3) is fairly extended. In particular, at velocities between 7.15 and 7.60 km s⁻¹, deep HNC (4-3) absorption can be discerned toward the whole extent of the 0.84 mm continuum, with almost all continuum emission absorbed. The extended HNC (4-3) absorption seen between 7.15 and 7.60 km s⁻¹ may result from outer envelope of 4A1 and 4A2 or even diffuse molecular gas located in the NGC 1333 cloud. Given that a velocity gradient is observed between 4A1 and 4A2 (see Section 4), we suspect that at large scale, a velocity gradient can be discerned as well because gas motions may take place from the inner to the outer envelope surrounding the IRAS 4A. The extended HNC (4-3) absorption, however, shows no sign of a velocity gradient across the extent of the IRAS 4A continuum. Therefore, we favor the HNC (4-3)absorption observed between 7.15 and 7.60 km s⁻¹ tracing an extended redshifted foreground layer, although the possibility of a common envelope of 4A1 and 4A2 or even diffuse molecular gas in NGC 1333 cannot be fully ruled out.

This foreground layer of material has previously been implied by Liseau et al. (1988) in CO (1–0) and by Yıldız et al. (2013) in O_2 (3₃–1₂). With *Herschel* observations of multiple water lines, Mottram et al. (2013) recently reported a low-density foreground absorption layer at $V_{\rm LSR}$ of 8.0 km s⁻¹,

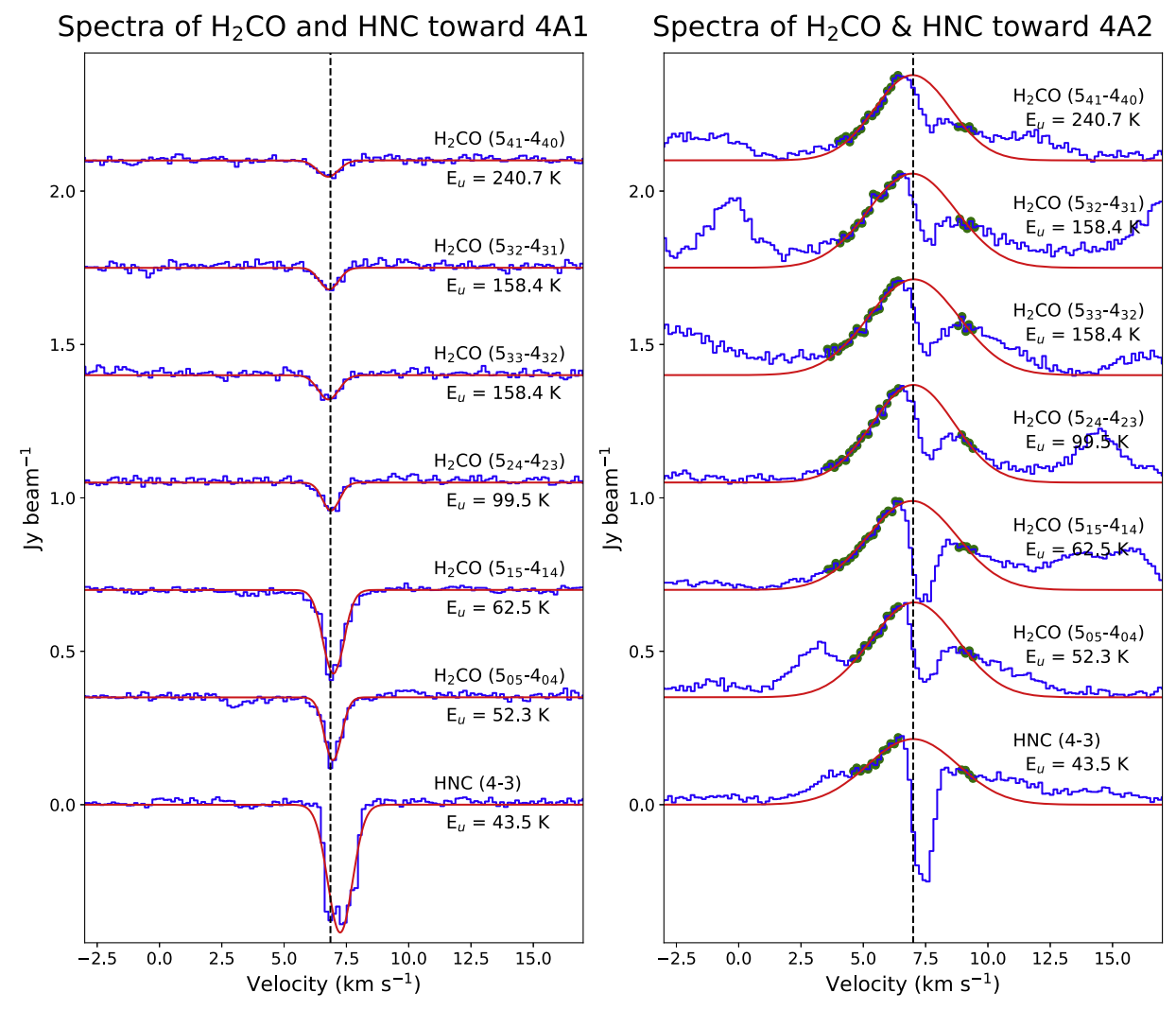


Figure 4. Continuum-subtracted spectra of the six H_2CO lines as well as HNC (4–3) toward the central positions of 4A1 (left) and 4A2 (right) in the sequence of excitation from bottom to top. The transitions and the corresponding upper-state excitation energies are also labeled. The fitted Gaussian profiles are overlaid. Note that in the case of 4A2, only partial data points (marked as green points) are used in the fitting. Data points that are contaminated by infall or outflow motions are excluded from the fitting. The dotted line denotes the systemic velocity of 4A1 (left) and 4A2 (right) at 6.86 and 7.00 km s⁻¹, respectively, as estimated from the average central line velocity of the six H_2CO lines. Note that the brightness temperatures inferred from the observed peak continuum are 57 and 42 K toward 4A1 and 4A2, respectively (1 K is equivalent to \sim 7 mJy beam⁻¹).

redshifted by about 1 km s⁻¹ with respect to the systemic velocity of IRAS 4A. Mottram et al. (2013) further argued that both the infall in the IRAS 4A envelope and the foreground layer are required in their model spectra calculations to reproduce the observed water line profiles well. Limited by coarse angular resolutions, the above observations unfortunately were not able to differentiate gas kinematics between 4A1 and 4A2 from the observed line profiles. We conclude that HNC (4-3) absorption traces not only the dense gas immediately surrounding 4A1, but also this previously identified redshifted foreground material. This causes the HNC (4-3) line width to become broader than that of the H₂CO lines. The absorption of the foreground layer also shifts the HNC (4-3) central line velocity redward. This foreground layer could be part of a converging flow that is involved in the formation of the dense gas that collapsed into the IRAS 4A system or an independent gas layer.

Compared with the HNC (4-3) transition, the observed H_2CO transitions listed in Table 1 all have higher energy levels and effective excitation density (Shirley 2015), and hence are

unlikely to trace the foreground gas. For example, at a gas temperature of 20 K, the effective excitation density of HNC (4–3) is $2.4\times10^5\,\mathrm{cm}^{-3}$ only, which is about an order of magnitude lower than that of $\mathrm{H_2CO}~5_{05}$ – $4_{04}~(3.8\times10^6~\mathrm{cm}^{-3})$ and $\mathrm{H_2CO}~5_{15}$ – $4_{14}~(2.3\times10^6~\mathrm{cm}^{-3})$ (Shirley 2015). The remaining four observed $\mathrm{H_2CO}$ transitions have even higher energy levels and effective excitation densities. Indeed, the absorption signatures between 7.15 and 7.60 km s $^{-1}$ in HNC (4–3) are not evident in the observed $\mathrm{H_2CO}$ transitions, indicating that $\mathrm{H_2CO}$ probes material mainly in the close vicinity of 4A1.

Figure 5 presents the integrated intensity maps (integrated from 5.95 to $8.05 \, \mathrm{km \, s^{-1}}$) of HNC (4-3) and five observed H₂CO transitions toward 4A1. The absorption features of all five H₂CO transitions detected toward 4A1 are relatively compact, in particular for the high-excitation lines. A weak emission component to the southeast of the centroid position is most likely related to the outflowing gas mentioned in the previous section. In contrast, the absorption seen in HNC (4-3) is fairly extended, as mentioned above. These H₂CO

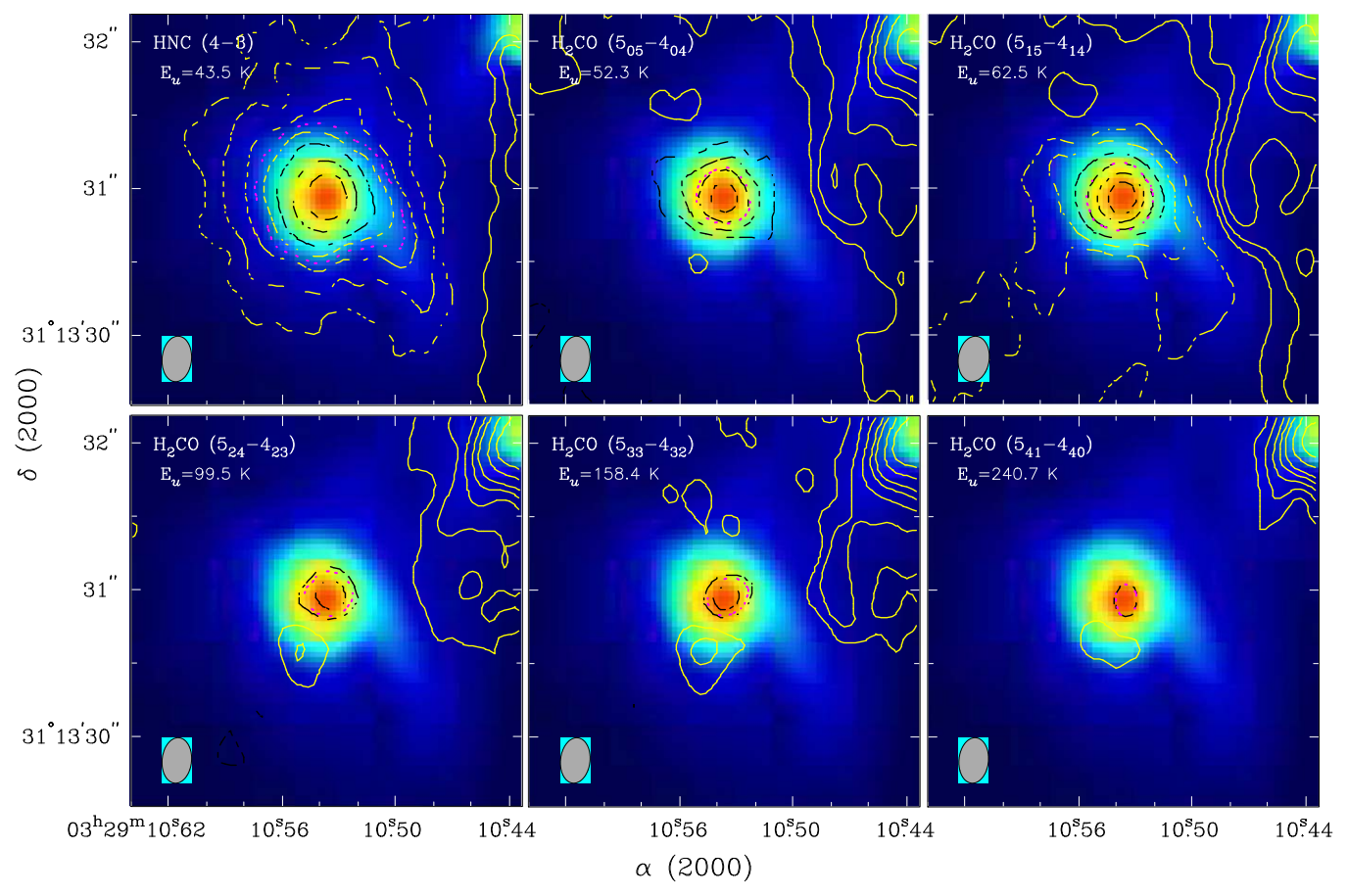


Figure 5. Contour plots of the integrated intensity maps of HNC (4-3) and various H_2CO lines toward 4A1 integrated from 5.95 to 8.05 km s⁻¹. In each panel, the color scales present the 0.84 mm continuum shown in Figure 1 and the dark ellipse at the bottom left denotes the synthesized beam. The transitions are labeled in the top left corner of each panel. Solid contours are at 3, 6, 10, 15, 20, 30, and 40×10 mJy beam⁻¹ km s⁻¹, and dashed contours indicate -3, -6, -10, -15, -20, -30 and -40×10 mJy beam⁻¹ km s⁻¹. In each panel, the red contour represents 50% of the peak absorption.

lines show no sign of a velocity gradient in the E–W direction, i.e., the axis perpendicular to the outflow associated with 4A1 shown in Figures 2 and 3.

What are the physical properties of the H₂CO absorption gas? With multiple H₂CO transitions captured, we can estimate to the zeroth order approximation, a mean or representative gas temperature using the rotation diagram analysis (Turner 1991) by assuming the observed H₂CO transitions in 4A1 are optically thin. We regard the continuum emission as the "background" in the radiative transfer (RT) equation, and the absorbing molecular line forms in a uniform "foreground" layer. Following the analysis presented in Sahu et al. (2019), a rotational temperature of 79 K and a H₂CO column density of 3×10^{14} cm⁻² toward the 4A1 centroid are estimated. For comparison, Sahu et al. (2019) reported at the 4A1 center rotational temperatures of \sim 60 K and \sim 140 K for the observed CH₃OH and ¹³CH₃OH transitions, respectively, and a CH₃OH column density of $\sim 10^{17}$ cm⁻². Assuming a typical fractional abundance of CH₃OH of 10^{-6} (Herbst & van Dishoeck 2009), the total column density of the absorbing COM (atmosphere) layer is estimated to be at the level of 10^{23} cm⁻². With a fractional abundance of H_2CO of 2×10^{-8} (Marzet et al. 2004), our study suggests a column density of $3 \times 10^{22} \text{ cm}^{-2}$ for the absorbing layer, in agreement with that estimated from the CH₃OH transitions by Sahu et al. (2019).

While it is desirable to obtain a temperature map in the close vicinity of 4A1 by applying the rotation diagram analysis to a

more extended area, the compact nature of the H₂CO absorption as well as the contamination from the outflowing gas limit the applicable extent extremely. For example, the three high-excitation H_2CO transitions (i.e., $5_{33}-4_{32}$, $5_{32}-4_{31}$, and $5_{41}-4_{40}$) are not detected at a radius beyond 0."25, equivalent to the synthesized beam size, away from the 4A1 center. At this radius, the detection of H₂CO 5₂₄-4₂₃ is also marginal, about 3–4 σ only. Regarding the two low-excitation H_2CO transitions (i.e., $5_{05}-4_{04}$ and $5_{15}-4_{14}$), although the absorption feature can be detected up to a radius of ~ 0.75 , the contamination from outflowing gas (in particular along the N-S direction) makes the line profiles non-Gaussian. As a consequence, we simply extend the estimate of gas temperature to four representative locations 0."25 to the N, S, E, and W of 4A1. With the three detected H₂CO transitions, the estimated gas temperatures are in a range of 45-60 K. The results appear to indicate a radial temperature gradient on the plane of sky.

4.2.2. The Line Feature toward 4A2

The right panel of Figure 4 presents the observed spectra of the six H_2CO transitions and HNC (4–3) toward the 4A2 centroid. Unlike a simple (absorption) Gaussian profile detected predominantly toward 4A1, the line profiles observed toward the 4A2 continuum centroid demonstrate more complicated features. The observed H_2CO as well as HNC (4–3) transitions all exhibit emission features, as shown in the

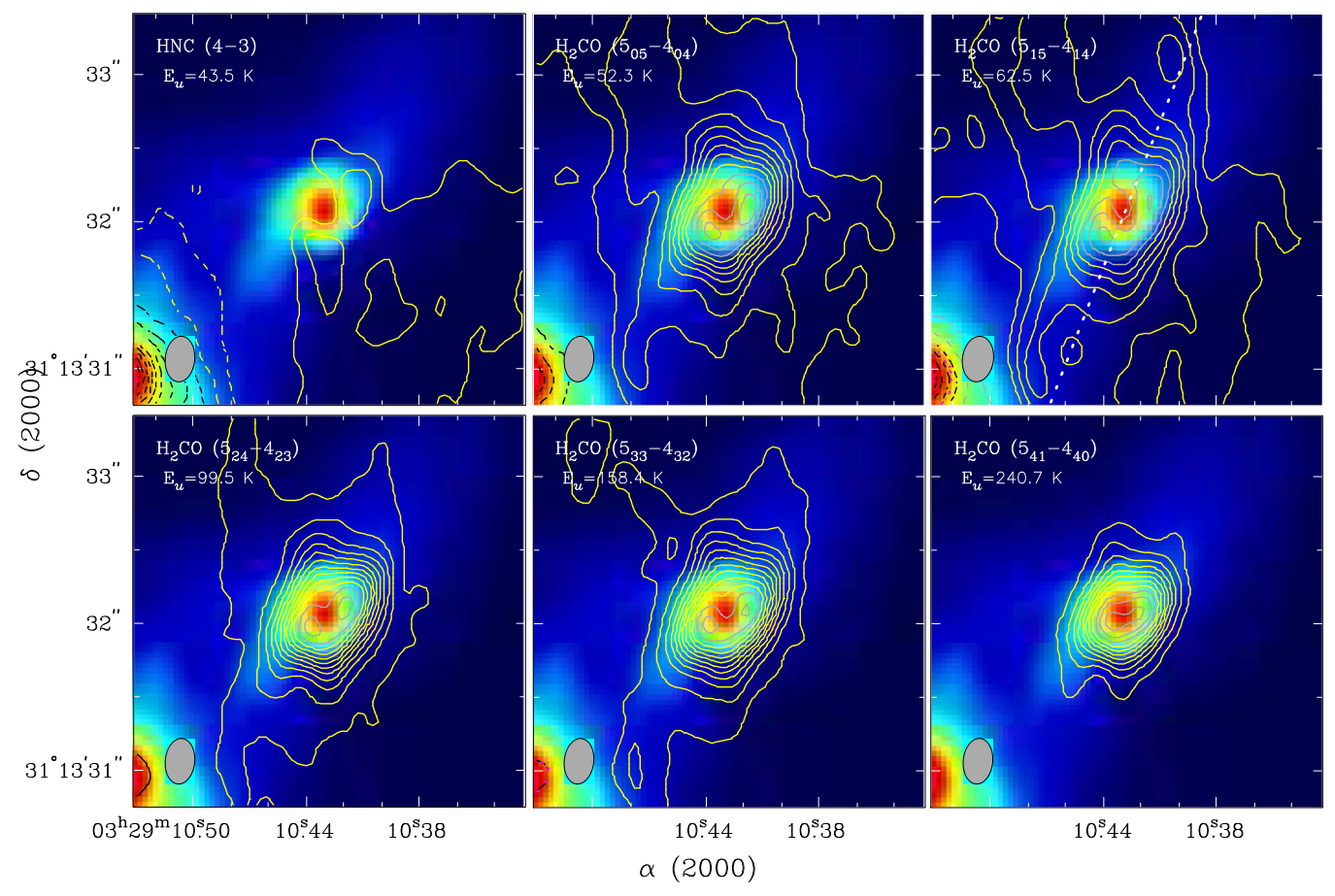


Figure 6. Contour plots of the integrated intensity maps of HNC (4–3) and various H_2CO lines toward 4A2 integrated from 5.95 km s⁻¹ to 8.05 km s⁻¹. In each panel, the color scales present the 0.84 mm continuum shown in Figure 1 and the dark ellipse in the bottom left corner denotes the synthesized beam. The transitions are labeled in the top left corner of each panel. Contours are at 4, 8, 12, ... 48×10 mJy beam⁻¹ km s⁻¹. The white dotted line shown in the panel of H_2CO $5_{1,5}$ – $4_{1,4}$ represents the axis of the position–velocity diagram plotted in Figure 8.

right panel of Figure 4. Absorption features are also detected toward the 4A2 center. Among these transitions, H₂CO 5₁₅–4₁₄ and HNC (4-3) demonstrate the inverse P-Cygni line profiles, i.e., absorption against continuum emission in redshifted velocity, and the remaining H₂CO lines exhibit asymmetric blue profiles. The observed line profile can be fit with a Gaussian shape when the low-velocity redshifted absorption channels are excluded. We again performed Gaussian profile fitting to extract the line parameters. The fitting profiles as well as the 4A2 systemic velocity of $7.00 \,\mathrm{km \, s^{-1}}$ estimated from the average fitted peak velocity are overlaid in the right panel of Figure 4. We note that the data points used in the fitting are marked as green points in Figure 4. As summarized in Table 2, the inferred line width is about $4.0\,\mathrm{km\,s^{-1}}$, significantly broader than that estimated toward 4A1 of about 0.90 km s only. The estimated central line velocities are in agreement with each other, i.e., they lie all in the range of $6.96-7.02 \,\mathrm{km \, s^{-1}}$. Another noticeable signature of the observed profiles is that all H₂CO transitions display similar peak intensities of \sim 43 K (equivalent to \sim 0.3 Jy beam⁻¹, or 85 K when the continuum emission is included), indicating the optically thick nature of these H₂CO transitions. This optically thick behavior toward 4A2 center has been revealed by Sahu et al. (2019), although the authors reported a slightly lower brightness temperature of 75 K (line + continuum), likely due to an intensity dilution in the spectral domain. We did not attempt the rotation diagram analysis to gauge the gas

temperature of 4A2 because the H_2CO emission and absorption profiles are complex and the emission is opaque at the emission peaks, which will lead to drastically overestimated gas temperature.

Figure 6 presents the integrated intensity maps (integrated from 5.95 to $8.05 \,\mathrm{km \, s^{-1}}$) of HNC (4-3) and five observed H_2CO transitions toward 4A2. The integrated HNC (4-3) map does not reveal an evident feature because the emission and the foreground layer absorption roughly cancel each other out toward 4A2. The integrated intensity maps of H₂CO lines, on the other hand, all demonstrate strong emission features, with an elongated structure along a position angle of about -20° . Because 4A2 is associated with a disk-outflow system (Choi et al. 2010; Santangelo et al. 2015), the elongated structure can be naturally related to either the disk or the outflow. The direction of the elongated structure, however, is not aligned with that of the rotating disk around 4A2, which is oriented along a position angle of about 108°9 (Choi et al. 2010). The elongation is also slightly different from the observed outflow direction in the N-S direction shown in Figures 2 and 3. Given the presence of the outflow precession in 4A2, however, the small-scale outflow in the close vicinity of 4A2 may not necessarily be aligned in the N-S direction.

To examine in detail the gas kinematics on small scales, we present in Figure 7 the channel maps of H_2CO $5_{1,5}-4_{1,4}$ zoomed into the central (2".5) region of 4A2, as well as in Figure 8 the position–velocity diagram in H_2CO $5_{1,5}-4_{1,4}$, also

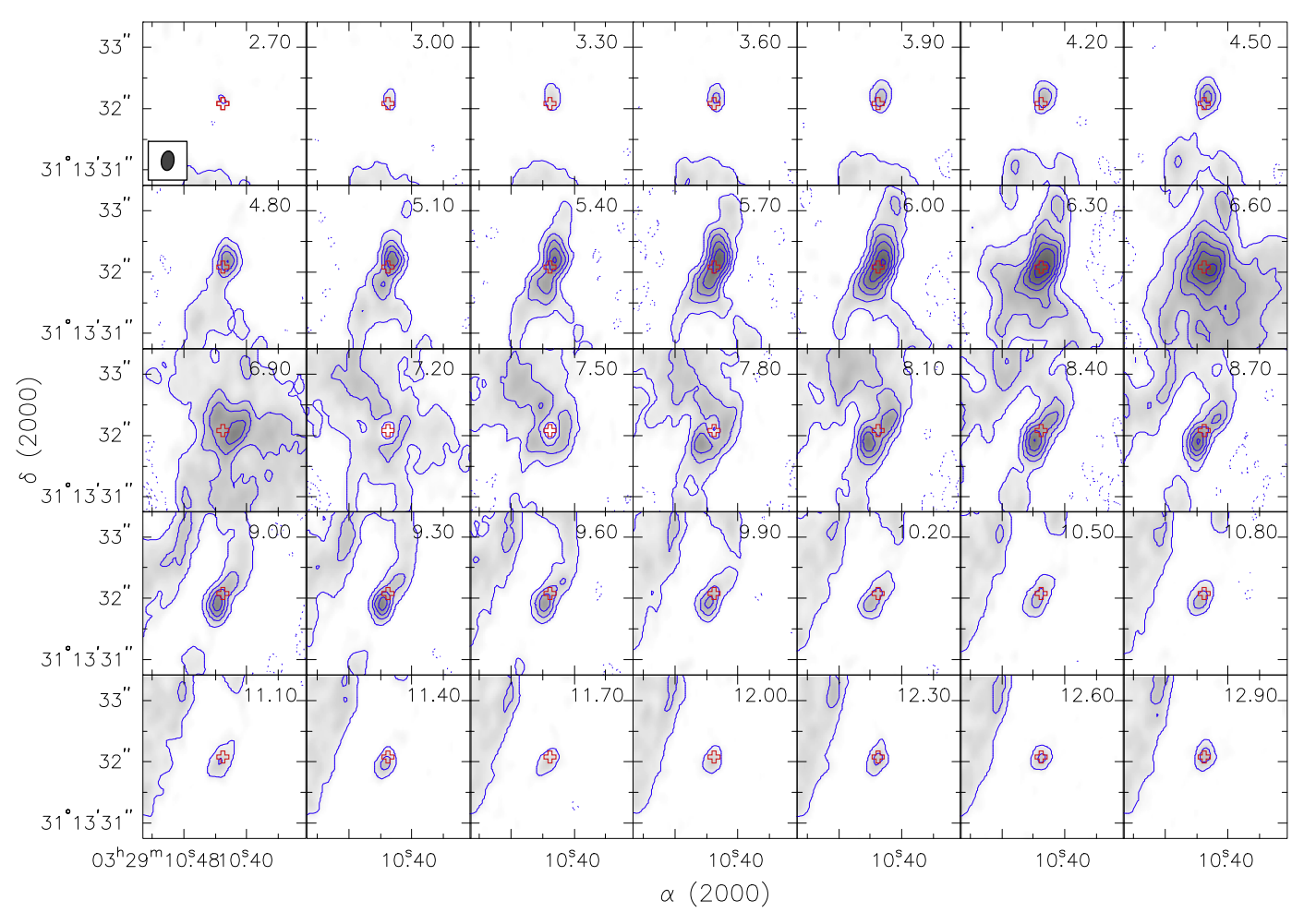


Figure 7. Channel maps of H_2CO 5_{15} – 4_{14} zoomed into the central region of 4A2. The LSR velocity of each channel is indicated in the upper right corner of each panel. The LSR velocity of the 4A2 system is 7.00 km s⁻¹. Contours are at 4, 11, 18, 25, 32 and 39 × 7 mJy beam⁻¹. The dark ellipse in the bottom left corner of the first panel denotes the synthesized beam. In each panel, the red cross marks the position of the 4A2 compact component (Sahu et al. 2019). At a scale of \sim 1", an outflow along the north-northwest to south-southeast direction can be discerned.

centered at 4A2. The most notable feature shown in Figure 7 is at a scale of $\sim 1''$ an outflow oriented from north-northwest to south-southeast. The H₂CO gas kinematic structure, as revealed by the position-velocity diagram in the direction of the smallscale outflow (at a position angle of $-21^{\circ}.5$) shown in Figure 8 is far more complicated, however. The position-velocity diagram exhibits a velocity gradient with redshifted emission in the NNW and blueshifted emission on the SSE side, which connect further to the large-scale N-S outflows. On the other hand, a separate emission component with a nearly reversed velocity gradient that is even stronger in brightness is also revealed in Figure 8. While an outflow cone lying nearly in the plane of sky may result in both blue- and redshifted gas emission along the same line of sight, the disparate brightness and extent of the observed emission features do not seem to support this picture. Most recently, C.-Y. Chuang et al. (2019, in preparation) witness similar morphological and kinematic structures in CO and SO emission—a more extended emission with a velocity gradient aligned with the outflow and a compact $(\sim 1'')$ in diameter), perhaps flattened component with a reversed velocity gradient. They interpret the latter component as a rotating envelope and explain the bending outflow in the framework of magnetic fields that are misaligned from the initial rotation axis. Regardless of the interpretation, the

elongated emission shown in Figure 6 is contributed by this compact component.

As mentioned above, the spectral profiles of H₂CO toward 4A2 exhibit either the inverse P-Cygni or asymmetric blue profiles, both indicating the presence of inward motion in 4A2. The integrated intensity maps also show signatures of the infalling gas toward 4A2 because voids of H₂CO emission toward the 4A2 centroid can be clearly discerned in Figure 6. We note that such a void morphology can be seen in the integrated intensity map of low-excitation CH₃OH also (i.e., Figure 1b in Sahu et al. 2019). The channel maps shown in Figure 7 reveal an even clearer absorption feature from about 7.0 to 7.90 km s⁻¹, with a compact (~ 0.75) ring-like emission structure symmetrically centered at 4A2. Such a ring-like morphology is detected not only in H₂CO 5_{1,5}-4_{1,4} but also in other observed H₂CO transitions. With a systemic velocity of 7.0 km s⁻¹, the redshifted absorption signature most likely traces the inward motion of 4A2. We discuss in Section 5.4 the physical properties of the possible infalling gas in 4A2.

5. Discussion

5.1. Gas Kinematics in 4A as a Whole

The presence of the well-collimated bipolar outflows in 4A strongly implies that its embedded young binary stars are both

Position - Velocity Diagram

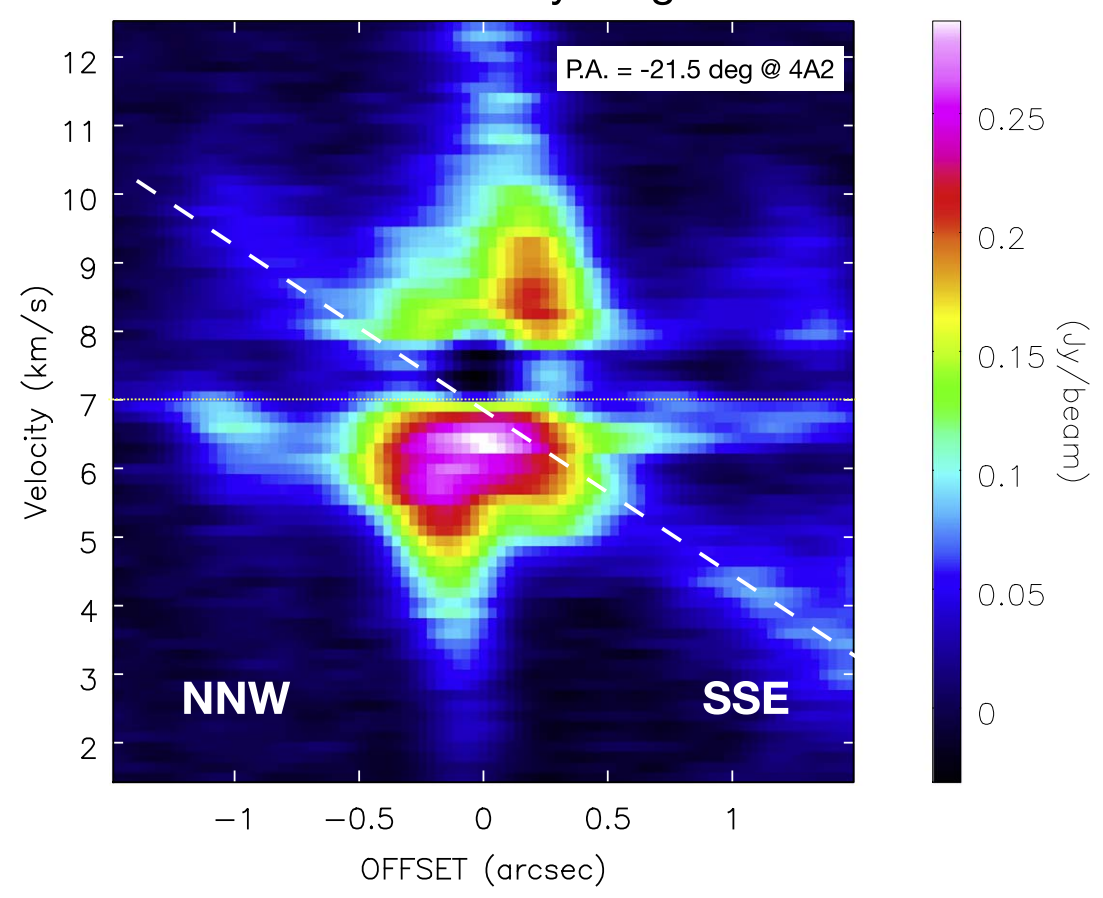


Figure 8. Position–velocity diagram in $H_2CO\ 5_{1,5}$ – $4_{1,4}$ along the P.A. of $-21^{\circ}5$ centered at 4A2. The white dashed line labels the small-scale outflow along the north-northwest to south-southeast direction. The dotted horizontal line denotes the 4A2 systemic velocity of $7.00 \ \text{km s}^{-1}$.

still in an active accretion phase. Hence, one may expect to identify signatures of inward gas motion within the 4A region. Such signatures have been reported in previous studies. For example, one piece of evidence is the detection of the inverse P-Cygni profiles in H_2CO ($3_{12}-2_{11}$) with the PdBI observations at a resolution of $\sim 2''$ (Di Francesco et al. 2001). By matching the observed H_2CO profile with a two-layer RT model, Di Francesco et al. (2001) deduced an infall velocity toward 4A of 0.68 km⁻¹.

To compare the H_2CO spectral features of our ALMA observations with the previous PdBI results, we downgrade the spatial resolution of our datacube to 2'', comparable to that of the PdBI observations, by tapering the visibilities during imaging. Indeed, we present in Figure 9 an inverse P-Cygni signature in our ALMA 2'' H_2CO 5_{15} – 4_{14} spectral profile that is similar to the PdBI H_2CO 3_{12} – 2_{11} results. A broad line wing, most likely associated with the outflowing gas, in both red- and blueshifted parts can be discerned in both transitions, although it is stronger and broader in our case. We note that the bright narrow blueshifted emission peak at \sim 6.6 km s⁻¹ is contributed by 4A2.

Recently, *Herschel* WISH observations in multiple water transitions toward IRAS 4A also suggested infall motion in the IRAS 4A region as a whole. Through a series of studies (Jørgensen et al. 2002; Maret et al. 2004; Kristensen et al. 2012; Mottram et al. 2013), a detailed physical model of the region was constructed to interpret the observations. The physical model

parameters can be summarized as follows: density $n=3.05\times10^9~{\rm cm}^{-3}\times(r/33.5~{\rm au})^{-1.8};$ temperature $T=1.83\times(r/100~{\rm au})^{-2}+47.5\times(r/100~{\rm au})^{-1}+51.7\times(r/100~{\rm au})^{-0.4};$ infall velocity $v_{\rm inf}=v_{1000}\times(r/1000~{\rm au})^{-0.5},$ where $v_{1000}=1.1~{\rm km~s}^{-1};$ a turbulence velocity of 0.4 km s $^{-1};$ inner and outer boundary $r_{\rm in}=33.2~{\rm au}$ and $r_{\rm out}=11,200~{\rm au};$ a jump in formaldehyde fractional abundance with the jump occurring at the radius where the dust temperature reaches 100 K, i.e., $X({\rm H_2CO})=2\times10^{-10}~{\rm for}~r>r_{100~{\rm K}},$ and $2\times10^{-8}~{\rm for}~r< r_{100~{\rm K}},$ where $r_{100~{\rm K}}\sim100~{\rm au}$ with the above-mentioned temperature profile. In this particular model, the infall velocity at a radius of 1000 au (i.e., $v_{\rm inf}~(r)=v_{1000}\times(r/1000~{\rm au})^{-0.5})$ is estimated to be 1.1 km $^{-1}$ (Mottram et al. 2013). We note that these modeling efforts, all based on single-dish observations which did not have sufficient angular resolution to resolve apart 4A1 and 4A2, only considered the IRAS 4A region as a single one-dimensional spherically symmetric collapsing core.

5.2. Radiative Transfer Modeling Exercises for 4A1

When observed at a higher (\sim 0."25) angular resolution with ALMA, the H₂CO and HNC transitions toward the 4A1 center, as mentioned in Section 4.2.1, display distinctly different behavior from those acquired by single-dish observations. They are mainly Gaussian-like profiles predominantly in absorption, with typical line widths of only \sim 1 km s⁻¹. Furthermore, contrary to the expectation from the physical model outlined above, based on which a high-velocity (3–5 km s⁻¹) infalling

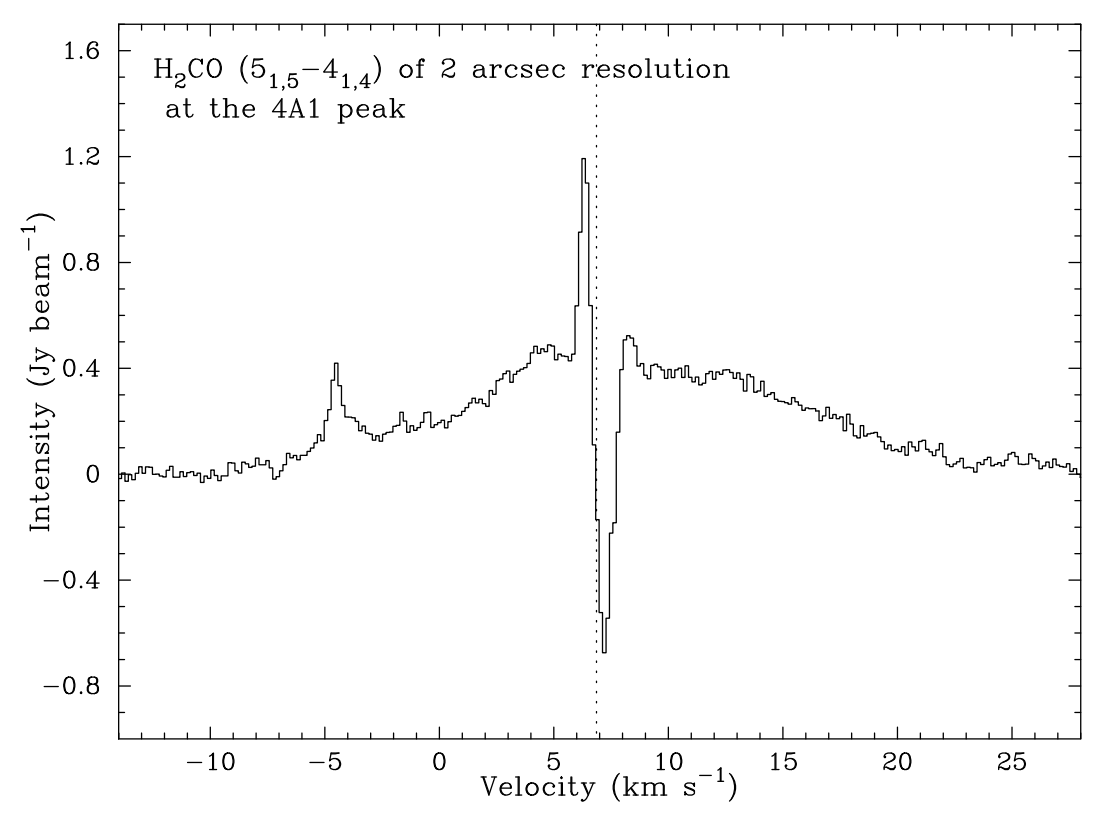


Figure 9. Spectra of $H_2CO\ 5_{1,5}$ – $4_{1,4}$ toward the central position of the 4A1 continuum with tapering the visibilities during imaging to 2" resolution. The dotted line denotes the 4A1 systemic velocity of 6.86 km s⁻¹. Although the spectral profiles are inverse P-Cygni-like, the redshifted absorption feature at \sim 7.2 km s⁻¹ and the blueshifted component peaking at \sim 6.6 km s⁻¹ come from 4A1 and 4A2, respectively.

signature should be present, the observed profiles show no sign of (redshifted) infalling gas with velocity $\gtrsim 0.5 \text{ km s}^{-1}$.

What causes this lack of high-velocity gas infall signature in H_2CO toward 4A1? As illustrated in Section 3, the dust continuum at 0.84 mm toward the 4A1 centroid is optically thick. Does the opaque dust emission prevent the detection of high-velocity infalling gas, which is expected to be located in the inner region of the 4A1 envelope? To investigate these effects further, we resort to RT modeling exercises.

We perform nonlocal thermal equilibrium (non-LTE) RT calculations with the SPARX⁴ package over the multiple H₂CO transitions. As an initial trial step, we adopt a toy 1D spherical collapsing-core model of IRAS 4A that incorporates the physical parameters inferred from previous studies as described above. To take the possible spatial filtering from the present ALMA observations into account, we simulated ALMA observations at its C43-3 and C43-5 configurations, which are the same configurations as those used in our ALMA observations by using the SPARX simulated data cubes as input model images. The beam size of the mock ALMA observations is almost the same as that of our observed ALMA results. Panel a of Figure 10 shows the simulated spectra of the three (para-) H_2CO transitions (i.e., $5_{05}-4_{04}$, $5_{24}-4_{23}$, and 5_{41} – 4_{40}) toward the continuum peak in the datacube obtained from the mock ALMA observations. The spectra of these three transitions exhibit both blueshifted emission features primarily associated with the infalling gas on the far side and redshifted

absorption features associated with the infalling gas on the near side. For the low-excitation transition (i.e., $5_{05}-4_{04}$), the simulated absorption signature is kinematically distinct in nature, with the "low-velocity" ($v \sim 1-3 \, \mathrm{km \, s^{-1}}$) feature mainly arising from gas located at the outer and cool ($T < 100 \, \mathrm{K}$) envelope at a relatively low infalling speed and the "high-velocity" ($v \sim 3-5 \, \mathrm{km \, s^{-1}}$) feature originating from gas in the inner and warm ($T > 100 \, \mathrm{K}$) collapsing core where the H₂CO fractional abundance is enhanced. The simulated spectra of the two high-excitation transitions, on the other hand, display absorption signatures in "high-velocity" only, due to insufficient pumping of H₂CO molecules up to high-excitation states in the outer and cool envelope.

The modeled spectral profiles, however, are significantly different from our observed ALMA results. Additionally, the modeled continuum brightness temperature is about a factor of 2 higher than the observed value. For a better understanding of how the adopted parameters affect the simulated spectral features, we performed a further set of RT calculations by varying the input density and infalling velocity. With the original adopted density parameter, the modeled dust continuum emission has a brightness temperature $T \sim 110$ K, higher than the observed value of 60 K. We tried two other high-density cases by increasing the original density profile to $3 \times$ and $10 \times$ values. These simulated spectra, as a consequence, reflect the effects of dust opacity variations in both continuum brightness and spectral features. The modeled continuum brightness shows a decreasing trend with increasing density (and hence column density). That is, the peak continuum brightness T_b is about 110 K, 60 K, and 23 K for the calculations with $1\times$, $3\times$, and $10\times$ in density, repectively. The result is consistent with the fact that an increasing dust or gas

⁴ SPARX, which stands for Simulation Package for Astrophysical Radiative Transfer, is a program for RT calculation of molecular lines and continuum using a parallelized accelerated Monte Carlo algorithm over full 3D nested grids (S.-Y. Liu et al. 2019, in preparation).

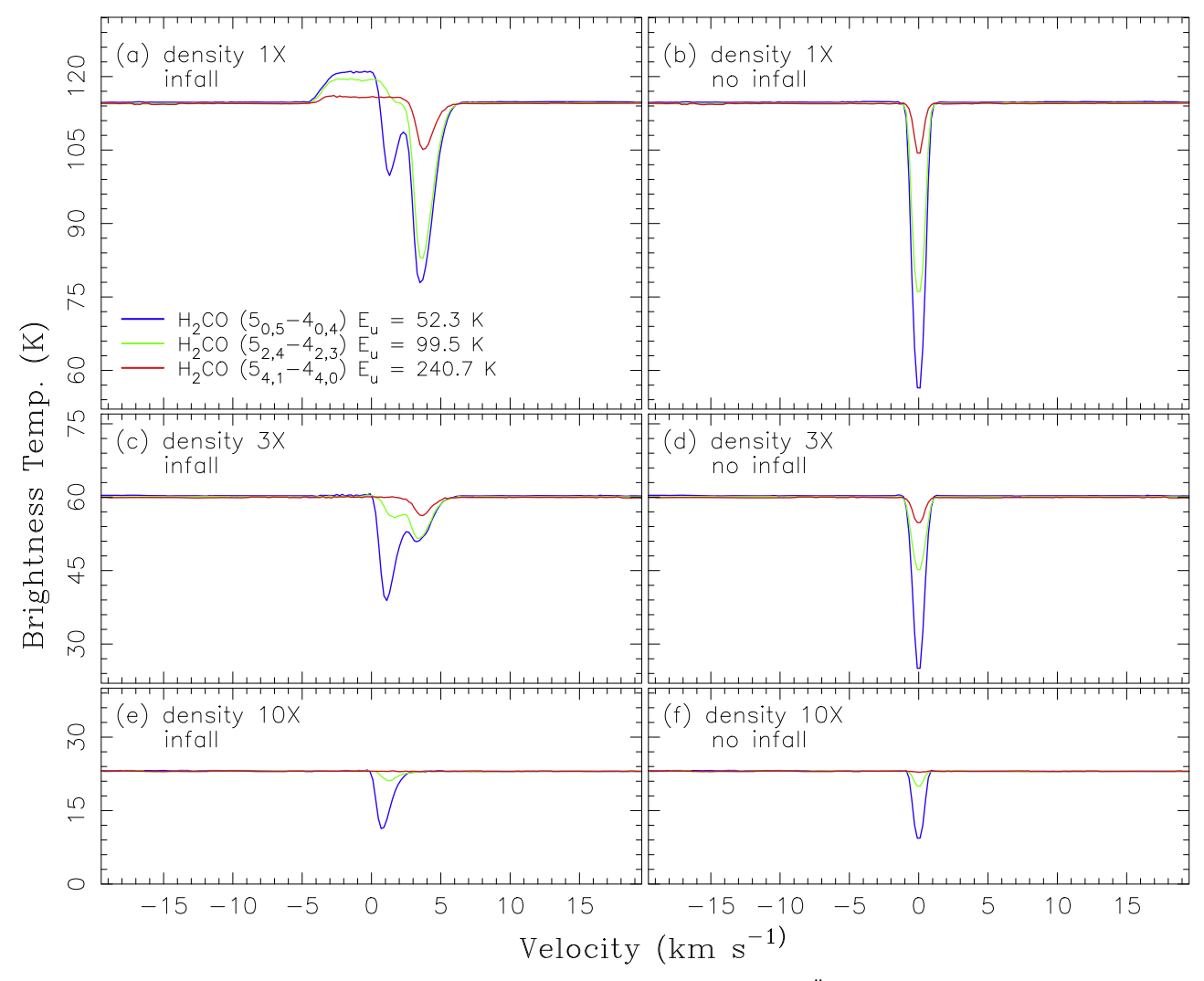


Figure 10. Modeled spectra of H_2CO 5_{05} - 4_{04} (blue), 5_{24} - 4_{23} (green), and 5_{41} - 4_{40} (red) toward the central 0.25 region of IRAS 4A with our SPARX calculations. Panel (a) presents simulated spectra of a toy 1D spherical collapsing-core model incorporating the physical parameters inferred from previous studies as described in Section 5.1. Panels (c) and (e): same as panel (a), but increasing the original density profile to $3\times$ and $10\times$ values, respectively. Panels (b), (d), and (f): same as panels (a), (c), and (e), respectively, but no infalling motion. The results demonstrate that high-excitation transitions are ideal tracers for probing faster infalling gas located closer to the central object. The absorption feature at 3-5 km s⁻¹ from faster inner infalling gas can be clearly discerned at 0.25 resolution.

density shifts the optically thick surfaces of the dust continuum to the outer and cooler regions. Regarding the spectral features, as shown in Figure 10, the contrast between high- $(v \sim 3-5 \text{ km s}^{-1})$ and low- $(v \sim 1-3 \text{ km s}^{-1})$ velocity absorption in these simulated spectra also demonstrates a trend with input density. The "high-velocity" feature is the dominant component in the $1\times$ density case and vanishes in the $10\times$ density case. In contrast, the "low-velocity" feature is the minor component in the 1× density case but becomes the dominant component in the $3\times$ density case as the faster infalling material closer to the central star becomes optically thicker and thus contributes less to the absorption. Since "high-velocity" absorption features trace infalling gas located at the inner and warm envelope, the decreasing trend of the "high-velocity" absorption depth with dust or gas density is the result of increasing dust obscuration of the inner and warm envelope. Meanwhile, no clear dust opacity effect can be discerned in the modeled "low-velocity" absorption signatures. Finally, we also set up RT models with non-infalling motion in the 4A1 envelope for comparison purposes. The modeled spectral profiles in these cases (shown in panels (b), (d), and (f) of

Figure 10) display absorption features only at the systemic velocity, as expected.

In short, our RT calculations indicate that although dust opacity plays an essential role in obstructing the detection of "high-velocity" infalling gas, the "low-velocity" absorption feature should be readily captured when the infall profile following the fiducial model is considered. Our observed H₂CO profiles, however, lack such signatures of both high- and low-velocity infalling motions, which is puzzling. We discuss possible resolutions to this interesting puzzle next.

5.3. The Physical Structures of 4A1

The discrepancies between the observed and the modeled spectra of 4A1 suggest that the physical parameters inferred from earlier low-resolution observations and used in the toy models cannot be directly extrapolated down to the inner region of 4A1. We discuss below possible reasons for such differences. First, the actual inward motion may be significantly slower or the velocity profile is much shallower than that inferred by Mottram et al. (2013). The simulated spectra of the

 $3\times$ density case, which reproduce the observed continuum brightness well, exhibit "high-velocity" absorption features up to $4.0~{\rm km~s^{-1}}$ in relative velocity, arising from gas located at 75 au. Because our observations show no sign of (redshifted) infalling gas with velocity $\gtrsim 0.5~{\rm km~s^{-1}}$, we estimate that the radial inward motion at a radius of 75 au should be at least a factor of 8 slower than that extrapolated from the velocity structure deduced by Mottram et al. (2013). Using the parameters described above at the layer of 75 au, we further constrain the mass infall rate in 4A1 to be (at most) around $3\times 10^{-5}~M_{\odot}~{\rm yr^{-1}}$, which is about a factor of 5 lower than that obtained by Mottram et al. (2013) on the 1000 au scale.

In addition, the 1D collapsing-core model approximation most likely has to break down. On the large scale, there are multiple energetic bipolar molecular outflows. In the inner envelope, the existence of a rotating disk in the close vicinity of 4A1 is expected for launching the bipolar outflows. The presence of outflows and disks would call for a 2D or 3D description of the core and envelope structure surrounding 4A1. In this case, the actual gas accretion flowing onto the disk may not lie along the line of sight and hence escape detection through line absorption against the continuum.

What then is the origin of the H₂CO absorption material seen toward 4A1? Sahu et al. (2019) proposed two possible scenarios to account for their observational absorption signatures of COMs, including CH₃OH, CH₃OD, and CH₃CHO, toward 4A1. In their Scenario I, the COM absorption lines arise from a hot-corino-like atmosphere at the surface of an optically thick circumstellar disk around 4A1 viewed closely face on. Under this scenario, a high accretion rate in the disk is actually required. The active accretion helps to produce a hot and bright continuum background in the inner disk, as required by the absorption feature. With comparable temperature and column density estimated from the rotational diagram analysis described in Section 4.2.1, it is possible that the absorptions of CH₃OH and H₂CO both arise from a hot-corino-like atmosphere. The nearly face-on disk configuration in this picture naturally breaks down the 1D assumption, and the accretion flow onto the disk may be channeled mostly close to the plane of sky, as suggested above.

In Scenario II of Sahu et al. (2019), the absorption features arise from different layers of a temperature-stratified, dense envelope. All or part of the absorption features toward 4A1 may be optically thick, and hence their brightness at the absorption line core is equal to the foreground absorbing gas temperature. The absorption lines with different excitation temperatures form at different layers in a temperature-stratified envelope—the lower excitation line saturates at the outer cooler layer, while the higher excitation transition (not excited at the outer layer) becomes optically thick in the relatively inner and hotter region. The 1D RT calculations with no infall motion discussed above resemble the physical nature of this Scenario II. We note here that the rotational diagram analysis described in Section 4.2.1 requires the assumption that all observed transitions arise from the same region, and hence it contradicts Scenario II. High-resolution observations of disk tracers at low frequency may help to discriminate the two scenarios if the disk is not totally face on but slightly inclined.

5.4. Gas Kinematics in 4A2

As illustrated in Section 4.2.2, the line profiles for the H₂CO transitions toward the 4A2 continuum centroid are more

complicated. They exhibit both emission and absorption with characteristics resembling inverse P-Cygni or asymmetric blue-skewed profiles. Based on the position-velocity diagram (Figure 8), the emission part of the spectra (with a line width of \sim 4 km s⁻¹) originates from a compact (\sim 1"), perhaps flattened envelope. We fit the profile of this H₂CO emission component, as described in Section 4.2.2, and assigned the average fitted peak velocity of 7.00 km s⁻¹ as the systemic velocity of 4A2. This systemic velocity is consistent with the results of previous studies (López-Sepulcre et al. 2017; Sahu et al. 2019). In particular, the line profiles of HCOOCH₃, CH₃OCH₃, HCOOCH, HNCO, etc. toward 4A2 reported by López-Sepulcre et al. (2017) at 0".5-1" resolution are mostly Gaussian-like, with fitted peak velocities predominantly in range of 6.8 to 7.1 km s⁻¹.

Meanwhile, there is also an intriguing feature in the $\rm H_2CO$ integrated intensity maps toward 4A2. The position angle of the integrated emission appears to rotate from about $-21^{\circ}.5$ for the outer ($\sim 1''$ scale) lower level contours to about -60° (or 120°) for the inner ($\sim 0.''.4$ scale) higher level contours. Coincidentally, a rotating disk associated with 4A2 at a position angle of $\sim 110^{\circ}$ was suggested by the VLA subarcsecond (0.''.3) observations in NH₃ (2,2) and (3,3) (Choi et al. 2010). Assuming a Keplerian rotation, Choi et al. (2010) estimated a rotation velocity of $1.8~{\rm km~s}^{-1}$ at a radius of 25 au (after scaling their adopted distance to from 235 to 293 au), which implies a central object of about $0.08~M_{\odot}$.

Similar to the expectation for 4A1, one may also anticipate evidence for inward gas motion toward 4A2, given its association with a disk and outflow system. On one hand, with this adopted systemic velocity, the absorbing dips in the H₂CO spectra are indeed skewed toward the redshifted side and likely signatures of inward motion. On the other hand, these absorbing dips are relatively narrow, extending up to around $V_{\rm LSR} \sim 8~{\rm km~s^{-1}}$. As for the case for 4A1, these speeds are significantly slower than the anticipated inflow speed should the 1D collapsing-core model be extrapolated down to this scale. The lack of a proper description for the complex mixture of disk, outflow, and envelope components around 4A2 prevents us from formulating a full RT modeling experiment. Here we try to interpret the observed absorption or skewed profiles with another approach. We assume the fitted Gaussian profiles shown in the right panel of Figure 4 represent the spectral feature of a "model" without absorption. As a consequence, we can estimate the absorption opacity using the intensity difference between the model and the observed line profiles. With similar peak intensities of \sim 85 K, most H₂CO transitions are likely optically thick at the center velocity. The absorption opacity, however, could be significantly lower, in particular, off the line center. We estimate the line opacity of the absorption layer as a function of velocity for all the observed H₂CO lines by assuming the optically thin case: $\tau(v) \simeq (1 - \exp(-\tau(v))) = ((I_{\text{line-model}}(v) + I_{\text{cont}}) - I_{\text{cont}})$ $(I_{\text{line-obs}}(v)+I_{\text{cont}}))/(I_{\text{line-model}}(v)+I_{\text{cont}})$, where I_{cont} , $I_{\text{line-obs}}$, and $I_{\text{line-model}}$ are the observed continuum intensity, the observed line intensity, and the intensity of the fitted Gaussian spectra shown in Figure 4, respectively. Figure 11 presents the estimated absorption opacities of the six observed H2CO transitions as a function of gas velocities (V_{LSR}) toward the 0.84 mm continuum peak of 4A2. As shown in Figure 11, for all the transitions the highest opacities are in the range of $7.4-7.8 \,\mathrm{km \, s^{-1}}$. With the assigned systemic velocity of

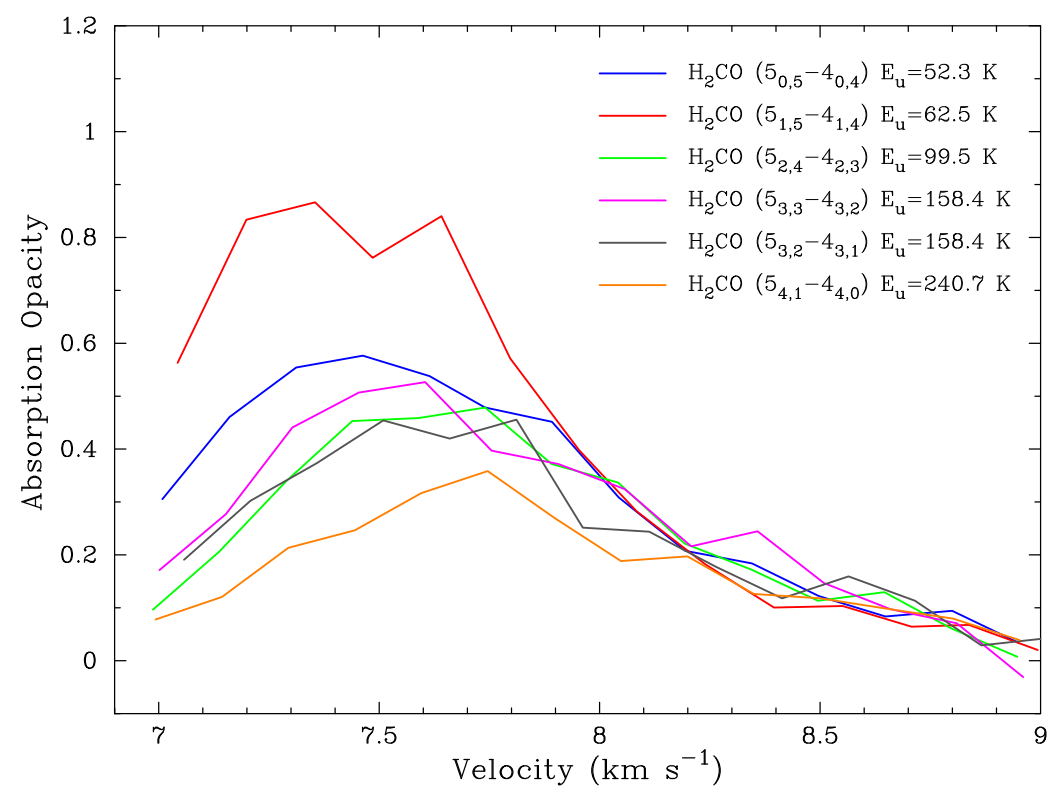


Figure 11. Absorption opacities of the six observed H_2CO transitions as a function of gas velocities (V_{LSR}) toward the 0.84 mm continuum peak of the 4A2. Given a systemic velocity of 7.0 km s⁻¹, there appears to be a trend that the relative velocity of the peak opacity increases from 0.4 to 0.8 km s⁻¹ with the line excitation. The trend is consistent with the picture that the high-excitation line traces the higher infall velocities better closer to the central young star.

 $7.0 \, \mathrm{km \, s^{-1}}$, interestingly, there appears to be a trend that the relative velocity of the peak opacity increases from 0.4 to $0.8 \, \mathrm{km \, s^{-1}}$ with the line excitation. The trend is consistent with the picture that the high-excitation line traces the higher infall velocities better closer to the central young star.

Given that the excitations of the observed H_2CO transitions are in range of 50–240 K, we adopt a gas temperature of ~ 100 K for the observed infalling material in 4A2. If the density and temperature structures of the 4A2 inner envelope are similar to those inferred from earlier low-resolution observations and used in our toy models mentioned in Section 5.1, then the observed inward material of $T \sim 100$ K is located at a layer of 100 au with a density of 4.3×10^8 cm⁻³. Together with an infall velocity of 0.4–0.8 km s⁻¹, we anticipate a mass infall rate of $(3.1-6.2)\times 10^{-5}~M_{\odot}~\rm yr^{-1}$ at the layer of 100 au in 4A2. For comparison, Mottram et al. (2013) estimated a mass infall rate of $1.54\times 10^{-4}~M_{\odot}~\rm yr^{-1}$ for the 4A system on the 1000 au scale.

5.5. The Configuration of the IRAS 4A System

Figure 12 presents a schematic illustration of the IRAS 4A system. The cartoon provides connections between the observational results and the interpretations presented in this paper and in the literature, especially Mottram et al. (2013) and Sahu et al. (2019). On the large scale, the available data indicate that there are (at least) two types of absorbers. The first is a cold, low-excitation layer of molecular gas located between the IRAS 4A system and the observer, with an extent covering both 4A1 and 4A2. This layer can be discerned in our ALMA HNC (4–3) results and the low-excitation H_2O transitions (i.e., 1_{10} – 1_{01} , 1_{11} – 0_{00} , and 2_{12} – 1_{01}) reported by

Mottram et al. (2013). It appears that this component is moving toward the IRAS 4A system at a speed of $\sim 0.5-0.8 \, \mathrm{km \, s^{-1}}$, i.e., supersonically with a Mach number of about 3–4 for a gas temperature of $\sim 10 \, \mathrm{K}$. This layer could be part of a converging flow that is involved in the formation of the dense gas that collapsed into the IRAS 4A system or just an independent gas layer. The converging flow may result from the collision between the NGC 1333 main cloud and a turbulent cell, as introduced by Dhabal et al. (2019, see their Fig.18). The second absorber is identified in $\mathrm{H_2O}$ (202– $\mathrm{1_{11}}$) as part of the envelope of the IRAS 4A system (Mottram et al. 2013). The authors conclude that this water line comes from a distance of $\gtrsim 1000 \, \mathrm{au}$ from the 4A system, suggesting that this water layer should surround both 4A1 and 4A2 given their (projected) separation of only $\sim 500 \, \mathrm{au}$.

On the small scale, simple symmetric spectral profiles in absorption toward the 4A1 dust continuum centroid have been detected in multiple H₂CO transitions presented here, as well as CH₃OH and several COMs reported by Sahu et al. (2019). With no sign of (redshifted) infalling gas with velocity \gtrsim 0.5 km s⁻¹, we estimate that the radial inward motion at a radius of 75 au should at least be a factor of 8 slower than that extrapolated from the velocity structure deduced by Mottram et al. (2013). Two possible scenarios have been proposed by Sahu et al. (2019) to account for their observational absorption signatures of COMs toward 4A1. In their Scenario I, the COM absorption lines arise from a hot-corino-like atmosphere at the surface of an optically thick circumstellar disk around 4A1 that is viewed relatively face on. For Scenario II, the absorption features arise from different layers of a temperature-stratified dense envelope.

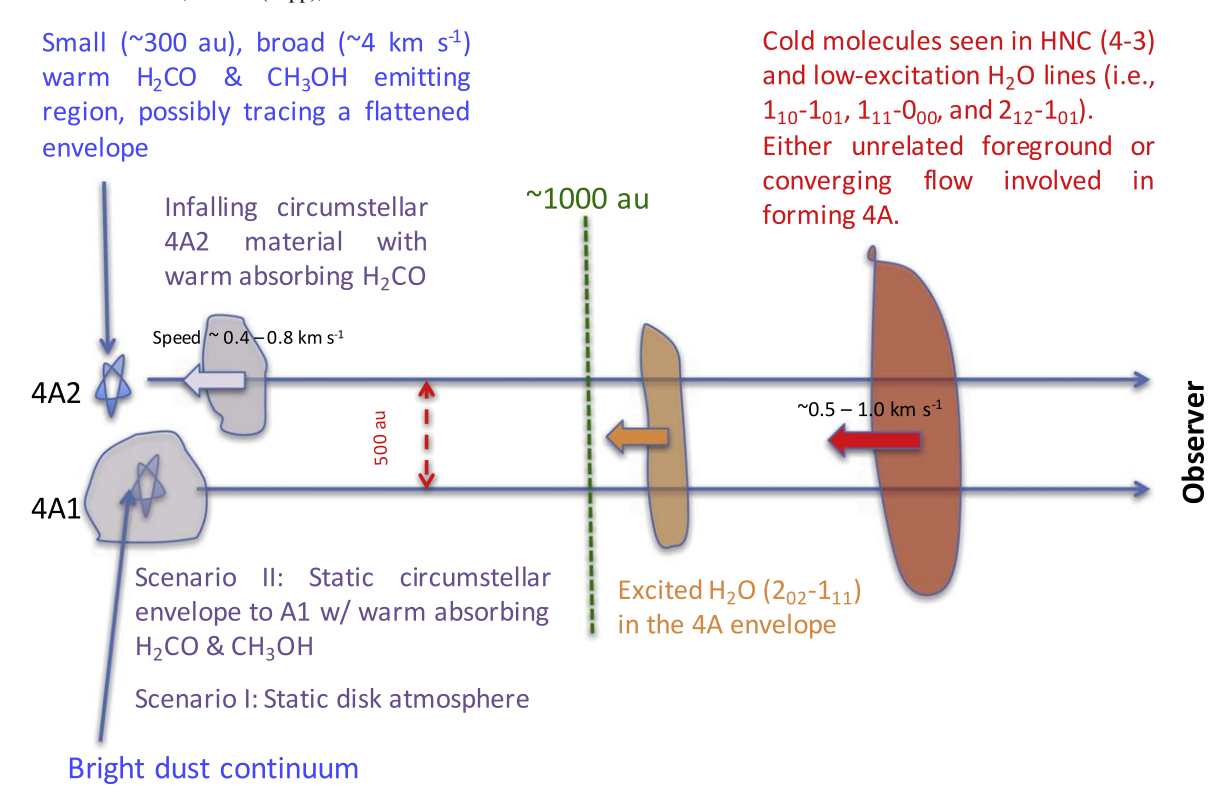


Figure 12. Schematic illustration of the IRAS 4A system inferred from the present ALMA observations as well as from the results presented by Mottram et al. (2013) and Sahu et al. (2019).

Component 4A2 is a known hot-corino-like source (Sahu et al. 2019, and reference therein). Given similar peak intensities, most observed transitions are likely optically thick at the center velocity in a resoltution of 0".25 (Sahu et al. 2019, and this study). With the adopted systemic velocity of $7.0 \,\mathrm{km \, s^{-1}}$, the absorbing dips in the H₂CO spectra are skewed toward the redshifted side and hence are likely signatures of inward motion. Similar to the case of 4A1, the observed infall velocity of 0.4–0.8 km s⁻¹ is significantly slower than the velocity that was extrapolated from the velocity structure deduced by Mottram et al. (2013). We estimate a mass infall rate of $(3.1-6.2) \times 10^{-5} M_{\odot} \text{ yr}^{-1}$ at the layer of 100 au in 4A2. This rate is somewhat lower than but comparable to that inferred by Mottram et al. (2013) on the 1000 au scale from H₂O absorption. The presence of infall in the inner envelope of the 4A system is consistent with the hourglass-shaped magnetic field observed by Girart et al. (2006) because the infalling gas is expected to drag the magnetic field lines into a highly pinched configuration (e.g., Galli & Shu 1993).

6. Summary

We report ALMA observations of NGC 1333 IRAS 4A, a young low-mass protostellar binary, in multiple H_2CO transitions as well as HNC (4–3) at a resolution of 0."25 (\sim 70 au) to investigate the gas kinematics of 4A1 and 4A2. Our main results can be summarized as follows.

- 1. On the large angular scale ($\sim 10''$), 4A1 and 4A2 each display a well-collimated outflow in the N–S direction, and an S-shaped morphology can be discerned in the outflow powered by 4A2.
- 2. With deep absorption between 7.15 and $7.60 \,\mathrm{km \, s^{-1}}$ covering the whole extent of the 0.84 mm continuum, our HNC

- (4-3) results confirm the existence of a previously inferred redshifted foreground layer.
- 3. On the small angular scale (\sim 0."3), 4A1 and 4A2 exhibit distinct spectral features toward the continuum centroid, with 4A1 showing simple symmetric profiles predominantly in absorption and 4A2 demonstrating rather complicated profiles in emission as well as in absorption.
- 4. With Gaussian-like profiles and typical line widths of 1 km s⁻¹, the observed H₂CO profiles toward 4A1 show no sign of (redshifted) infalling gas with velocity $\gtrsim 0.5 \,\mathrm{km \, s}^{-1}$. We perform non-LTE RT calculations with the SPARX package incorporating the physical parameters inferred from previous studies. The modeled profiles indicate that although dust opacity toward 4A1 plays an essential role in obstructing the detection of "high-velocity" (3–5 km s⁻¹) infalling gas, a "low-velocity" $(1-2 \text{ km s}^{-1})$ absorption feature should be readily detected. The discrepancies between the observed and the modeled spectra of 4A1 suggest that the physical parameters inferred from earlier low-resolution observations and used in the toy models cannot be directly extrapolated down to the inner region of 4A1. We constrain the mass infall rate in 4A1 to be (at most) around $3 \times 10^{-5} M_{\odot} \text{ yr}^{-1}$, which is about a factor of 5 lower than that obtained by Mottram et al. (2013) on the 1000 au scale.
- 5. For the kinematics of the 4A2 inner envelope, the absorbing dips in the $\rm H_2CO$ spectra are indeed skewed toward the redshifted side and are likely signatures of inward motion. These absorbing dips are relatively narrow, extending up to around $V_{\rm LSR} \sim 8~{\rm km~s^{-1}}$. As in the case for 4A1, these speeds are significantly slower than the anticipated inflow speed should the toy model be extrapolated down to this scale. We estimate a mass infall rate of $(3.1\text{--}6.2) \times 10^{-5}~M_{\odot}~{\rm yr^{-1}}$ at the layer of 100 au in 4A2. For comparison, Mottram et al. (2013)

estimated a mass infall rate of $1.54 \times 10^{-4} M_{\odot} \text{ yr}^{-1}$ for the 4A system on the 1000 au scale.

This paper makes use of the following ALMA data: ADS/ JAO.ALMA#2015.1.00147.S. ALMA is a partnership of ESO (representing its member states), NSF (USA), and NINS (Japan), together with NRC (Canada), MOST and ASIAA (Taiwan), and KASI (Republic of Korea), in cooperation with the Republic of Chile. The Joint ALMA Observatory is operated by ESO, AUI/NRAO and NAOJ. We thank the anonymous referee for the constructive suggestions. Y.N.S. thanks T.-H. Hsieh for providing the code used to infer spectral parameters and to make Figure 4. Y.N.S. acknowledges the support by the Minister of Science and Technology of Taiwan (MOST 107-2119-M-001-041 and MOST 108-2112-M-001-048). Z.Y.L. is supported in part by NASA 80NSSC18K1095 and NSF AST-1716259, 1815784, and 1910106. S.T. acknowledges a grant from JSPS KAKENHI grant No. JP18K03703 in support of this work. This work was supported by NAOJ ALMA Scientific Research grant No. 2017-04A.

ORCID iDs

Sheng-Yuan Liu https://orcid.org/0000-0003-4603-7119 Chin-Fei Lee https://orcid.org/0000-0002-3024-5864 Shigehisa Takakuwa https://orcid.org/0000-0003-0845-128X

References

```
Belloche, A., Parise, B., van der Tak, F. F. S., et al. 2006, A&A, 454, L51 Blake, G. A., Sandell, G., van Dishoeck, E. F., et al. 1995, ApJ, 441, 689 Bottinelli, S., Ceccarelli, C., Lefloch, B., et al. 2004, ApJ, 615, 354 Chen, X., Arce, H. G., Zhang, Q., et al. 2013, ApJ, 768, 110 Choi, M. 2005, ApJ, 630, 976 Choi, M., Kamazaki, T., Tatematsu, K., & Panis, J.-F. 2004, ApJ, 617, 1157 Choi, M., Kang, M., Tatematsu, K., Lee, J.-E., & Park, G. 2011, PASJ, 63, 1281 Choi, M., Tatematsu, K., & Kang, M. 2010, ApJL, 723, L34 Cox, E. G., Harris, R. J., Looney, L. W., et al. 2015, ApJL, 814, L28
```

```
Dhabal, A., Mundy, L. G., Chen, C.-yu, et al. 2019, ApJ, 876, 108
Di Francesco, J., Myers, P. C., Wilner, D. J., Ohashi, N., & Mardones, D. 2001,
   ApJ, 562, 770
Evans, N. J., II, Di Francesco, J., Lee, J.-E., et al. 2015, ApJ, 814, 22
Galli, D., & Shu, F. H. 1993, ApJ, 417, 243
Girart, J. M., Rao, R., & Marrone, D. P. 2006, Sci, 313, 812
Gonçalves, J., Galli, D., & Girart, J. M. 2008, A&A, 490, L39
Gueth, F., & Guilloteau, S. 1999, A&A, 343, 571
Herbst, E., & van Dishoeck, E. F. 2009, ARA&A, 47, 427
Jørgensen, J. K., Bourke, T. L., Myers, P. C., et al. 2007, ApJ, 659, 479
Jørgensen, J. K., Schöier, F. L., & van Dishoeck, E. F. 2002, A&A,
  389, 909
Ko, C.-L., Liu, H. B., Lai, S.-P., et al. 2019, arXiv:1909.09628
Kristensen, L. E., van Dishoeck, E. F., Bergin, E. A., et al. 2012, A&A, 542, 8
Lee, C.-F., Kwon, W., Jhan, K.-S., et al. 2019, ApJ, 879, 101
Lee, C.-F., Li, Z.-Y., Ho, P. T. P., et al. 2017, ApJ, 843, 27
Liseau, R., Sandell, G., & Knee, L. B. G. 1988, A&A, 192, 153
Liu, H. B., Lai, S.-P., Hasegawa, Y., et al. 2016, ApJ, 821, 41
Looney, L. W., Mundy, L. G., & Welch, W. J. 2000, ApJ, 529, 477
López-Sepulcre, A., Sakai, N., Neri, R., et al. 2017, A&A, 606, A121
Mardones, D., Myers, P. C., Tafalla, M., et al. 1997, ApJ, 489, 719
Maret, S., Ceccarelli, C., Caux, E., et al. 2004, A&A, 416, 577
McMullin, J. P., Waters, B., Schiebel, D., Young, W., & Golap, K. 2007, in
   ASP Conf. Ser. 376, Astronomical Data Analysis Software and Systems
  XVI, ed. A. R. Shaw, F. Hill, & D. J. Bell (San Fransico, CA: ASP), 127
Mottram, J. C., van Dishoeck, E. F., Schmalzl, M., et al. 2013, A&A, 558, 126
Myers, P. C., Evans, N. J., II, & Ohashi, N. 2000, in Protostars and Planets IV,
  ed. V. Mannings, A. P. Boss, & S. S. Russell (Tucson, AZ: Univ. Arizona
Ohashi, N., Hayashi, M., Ho, P. T. P., et al. 1997, ApJ, 475, 211
Ortiz-León, G. N., Loinard, L., Dzib, S. A., et al. 2018, ApJ, 865, 73
Persson, M. V., Harsono, D., Tobin, J. J., et al. 2016, A&A, 590, A33
Sahu, D., Liu, S.-Y., Su, Y.-N., et al. 2019, ApJ, 872, 196
Sakai, N., Sakai, T., Hirota, T., et al. 2014, Natur, 507, 78
Sandell, G., & Knee, L. B. G. 2001, ApJL, 546, L49
Santangelo, G., Codella, C., Cabrit, S., et al. 2015, A&A, 584, A126
Santiago-García, J., Tafalla, M., Johnstone, D., & Bachiller, R. 2009, A&A,
  495, 169
Segura-Cox, D. M., Looney, L. W., Tobin, J. J., et al. 2018, ApJ, 866, 161
Shirley, Y. 2015, PASP, 127, 299
Taquet, V., López-Sepulcre, A., Ceccarelli, C., et al. 2015, ApJ, 804, 81
Turner, B. E. 1991, ApJS, 76, 617
Wyrowski, F., Güsten, R., Menten, K. M., et al. 2012, A&A, 542, L15
Yıldız, U. A., Acharyya, K., Goldsmith, P. F., et al. 2013, A&A, 558, A58
Zapata, L. A., Loinard, L., Rodríguez, L. F., et al. 2013, ApJL, 764, L14
Zucker, C., Schlafly, E. F., Green, G. M., et al. 2018, ApJ, 869, 83
```